

Review

Bismuth Oxychloride Nanomaterials Fighting for Human Health: From Photodegradation to Biomedical Applications

Lili Wang ¹, Yang Liu ¹, Guoli Chen ¹, Mengyuan Zhang ¹, Xiaodong Yang ¹, Rui Chen ^{1,*} and Yan Cheng ^{2,*}

¹ Jilin Provincial Key Laboratory of Human Health Status Identification and Function Enhancement, College of Science, Changchun University, Changchun 130022, China; ccdxwll@163.com (L.W.); 18186842724@163.com (Y.L.); chenguoli2022@163.com (G.C.); zhang7225y@163.com (M.Z.); yangxd88@ccu.edu.cn (X.Y.)

² Engineering Research Center of Bioreactor and Pharmaceutical Development, Ministry of Education, College of Life Science, Jilin Agricultural University, Changchun 130118, China

* Correspondence: chenr@ccu.edu.cn (R.C.); ycheng@jlau.edu.cn (Y.C.)

Abstract: Environmental pollution and various diseases seriously affect the health of human beings. Photocatalytic nanomaterials (NMs) have been used for degrading pollution for a long time. However, the biomedical applications of photocatalytic NMs have only recently been investigated. As a typical photocatalytic NM, bismuth oxychloride (BiOCl) exhibits excellent photocatalytic performance due to its unique layered structure, electronic properties, optical properties, good photocatalytic activity, and stability. Some environmental pollutants, such as volatile organic compounds, antibiotics and their derivatives, heavy metal ions, pesticides, and microorganisms, could not only be detected but also be degraded by BiOCl-based NMs due to their excellent photocatalytic and photoelectrochemical properties. In particular, BiOCl-based NMs have been used as theranostic platforms because of their CT and photoacoustic imaging abilities, as well as photodynamic and photothermal performances. However, some reviews have only profiled the applications of dye degradation, hydrogen or oxygen production, carbon dioxide reduction, or nitrogen fixation of BiOCl NMs. There is a notable knowledge gap regarding the systematic study of the relationship between BiOCl NMs and human health, especially the biomedical applications of BiOCl-based NMs. As a result, in this review, the recent progress of BiOCl-based photocatalytic degradation and biomedical applications are summarized, and the improvement of BiOCl-based NMs in environmental and healthcare fields are also discussed. Finally, a few insights into the current status and future perspectives of BiOCl-based NMs are given.

Keywords: nanostructure; heterostructure; photodegradation; photodynamic therapy; biosensors; antibacterial; bioimaging



Citation: Wang, L.; Liu, Y.; Chen, G.; Zhang, M.; Yang, X.; Chen, R.; Cheng, Y. Bismuth Oxychloride Nanomaterials Fighting for Human Health: From Photodegradation to Biomedical Applications. *Crystals* **2022**, *12*, 491. <https://doi.org/10.3390/cryst12040491>

Academic Editor: Emmanuel Stratakis

Received: 14 March 2022

Accepted: 30 March 2022

Published: 1 April 2022

Publisher's Note: MDPI stays neutral with regard to jurisdictional claims in published maps and institutional affiliations.



Copyright: © 2022 by the authors. Licensee MDPI, Basel, Switzerland. This article is an open access article distributed under the terms and conditions of the Creative Commons Attribution (CC BY) license (<https://creativecommons.org/licenses/by/4.0/>).

1. Introduction

Human health has been threatened by environmental pollution and various diseases for a long time. Photocatalytic technology is recognized as one of the most promising technologies, which has been widely used in the treatment of environmental pollution. Recently, this technology has been used for disease diagnosis and therapy. Photocatalysis is a process of producing free electrons and holes, which can induce oxidation and reduction reactions [1–5]. When the energy of the incident light is greater than or equal to the band gap energy (E_g) of the semiconductor, the electrons from the valence band (VB) of the semiconductor can be excited and transfer to the conduction band (CB), leaving holes on the VB. The photogenerated electrons have strong reduction ability, while the holes have strong oxidation ability [6]. Therefore, an effective photocatalyst could be used for solving environmental and healthcare problems. For environmental pollution, a photocatalyst could produce both clean water and air due to the generation of reactive oxygen species (ROS), including superoxide radical ($O_2\bullet^-$), singlet oxygen (1O_2), and hydroxyl radical ($OH\bullet$), which can degrade both liquid and gaseous pollutants, such

as volatile organic compounds [7,8], antibiotics and their derivatives [9–12], heavy metal ions [13,14], microorganisms [15–17], and other water contaminants [18–21]. For theranostic platforms, on the one hand, photocatalysts could detect various biomarkers due to their photoelectrochemical (PEC) process for detecting pollutants and monitoring human health and food security [22,23]; on the other hand, some therapeutic agents are also derived from photocatalysts due to their light-triggered ROS generation abilities [24–26].

Thus far, plenty of inorganic nanomaterials (NMs) have been developed as photocatalysts. Among these NMs, bismuth oxyhalide (BIOX, X = Cl, Br, I) has attracted more attention because of its excellent photoelectronic properties [20,27–29]. The VB of BIOX is hybridized by O 2*p* and Bi 6*s* orbitals, and the CB is composed of a Bi 6*p* orbital. The internal electric field formed between layers can promote the effective separation of photogenerated electron holes, which plays a key role in improving the photocatalytic performance of BIOX NMs. As one of the most important and representative BIOX NMs, bismuth oxychloride (BiOCl) crystals belong to the tetragonal crystal system structure, the space group is P4/nmm (No. 129), and its crystal structure parameters are $a = b = 0.3891$ nm, $c = 0.7369$ nm, $\alpha = \beta = \gamma = 90^\circ$, $V_0 = 0.1108$ nm³, and $Z = 2$ [30]. From the van der Waals force analysis, there are weak non-bond orbits between the layers in the *c*-axis direction, but there is strong bonding in the (001) plane, the O²⁻ and Cl⁻ around Bi³⁺ form antisquare column coordination, the conical geometry structure with opposite direction and upper and lower asymmetry is formed, and the Cl⁻ layer is a positive square coordination. The next layer is the positive square O²⁻ layer, the Cl⁻ layer and the O²⁻ layers staggered at 45°, and intermediate sandwich Bi³⁺ layer. Under solar energy irradiation, electrons from the valence band Cl 3*p* orbital could jump to Bi 6*p* orbitals, and form photoinduction electrons and holes. The layered structure has enough space to polarize the atoms and the atomic orbits, prompt and induce the dipole moment, and effectively separate the electrons and holes, thus improving the photocatalytic performance.

BiOCl NMs show a unique layered structure, electronic properties, optical properties, good photocatalytic activity, and stability. Until now, a few reviews have systematically profiled the various photocatalytic applications, including dye degradation, hydrogen or oxygen production, carbon dioxide reduction, and nitrogen fixation [31–33]. The photocatalytic application of other bismuth oxychloride (such as Bi₁₂O₁₇Cl₂, Bi₁₂O₁₅Cl₆, Bi₃O₄Cl, Bi₄O₅Cl₂) phases has been developed as a research hot topic in recent years [34]. However, the biomedical application of these phases is rare. Therefore, this review was mainly focused on the BiOCl phase. In addition, no reviews have systematically profiled the relationship between BiOCl NMs and human health, especially the biomedical applications of BiOCl-based NMs, and a notable knowledge gap still exists in their potential property–activity relationship. In this review, we highlight the very recent progress of BiOCl-based NMs, from photocatalytic degradation to biomedical applications. We also summarize the improvement of BiOCl-based NMs in the environmental and healthcare fields. In particular, we propose and expand the application range of BiOCl, as well as other photocatalysts. At the end of this review, we give a few insights into the current status and future perspectives of this field.

2. BiOCl NMs Used for Treating Environmental Pollution

With the development of industry, the problems of water and air pollution are becoming more and more serious, which bring negative effects to human health. Some organic pollution and microorganisms in water pollution are difficult to remove by conventional technology. Photocatalytic oxidation has been widely studied to degrade organic pollutants and kill bacteria. In 2006, via a hydrolysis method, Zhang et al. synthesized BiOCl NMs, whose bandgap was measured to be 3.46 eV. With ultraviolet (UV) light irradiation, BiOCl could completely decompose methyl orange (MO) within 10 min, which exhibited higher efficacy than P25 NMs, showing an excellent photocatalytic degradation activity against MO [35]. Meanwhile, BiOCl NMs were also used to degrade other pollutants, such as pesticides, antibiotics, heavy metal ions, and microorganisms. Morphology regula-

tion and heterostructure formation are two common and effective strategies to improve photocatalytic degradation efficacy.

2.1. Improved Photodegradation Efficacy through Regulating Morphologies

As is well known, there is a close relationship between the morphology of nanostructure photocatalysts and their dye degrading activity. BiOCl NMs with various morphologies, including nanoplate, nanosheet, nanobelt, nanotube, microspheres, and microflowers, were fabricated to improve their photocatalytic efficacy. As a widely used surfactant, polyvinylpyrrolidone (PVP), was used for fabricating BiOCl NMs with different nanostructures [35]. Zhang et al. have used different surfactants as assembly reagents to investigate the influence of morphology as well as the photocatalytic activity. As shown in scanning electron microscope (SEM) images (Figure 1), without a surfactant, the main morphology is 2D nanoplates with an average size of 40 nm in thickness, while the 2D nanoplates could be self-assembled into uniform flower-like (Figure 1) and round pie-like (Figure 1) architectures when added to a PVP and bis(2-ethylhexyl) sulfosuccinate (AOT)/isooctane solution. They also proposed a possible growth mechanism. As shown in Figure 1, numerous tiny BiOCl crystalline nuclei appear first. Then, these tiny nuclei could grow into 2D nanoplates based on their inner crystallographic orientation. When adding PVP as the assemble reagent, these nanoplates could easily aggregate on these long chain polymers and form a 3D complex hierarchical structure. However, when using AOT as the surfactant, these nanoplates tend to constitute the final products of square plates due to the two hydrophobic chains of AOT. The building blocks of the flower-like BiOCl were cross-link nanoplates, while the pie-like were flat microplates. Compared with nanoplates, the flower-like BiOCl could effectively degrade different dyes, such as MO, rhodamine B (RhB), methene blue (MB), and ethylene violet (EV), with the irradiation of simulated sunlight due to its larger specific surface area [36].

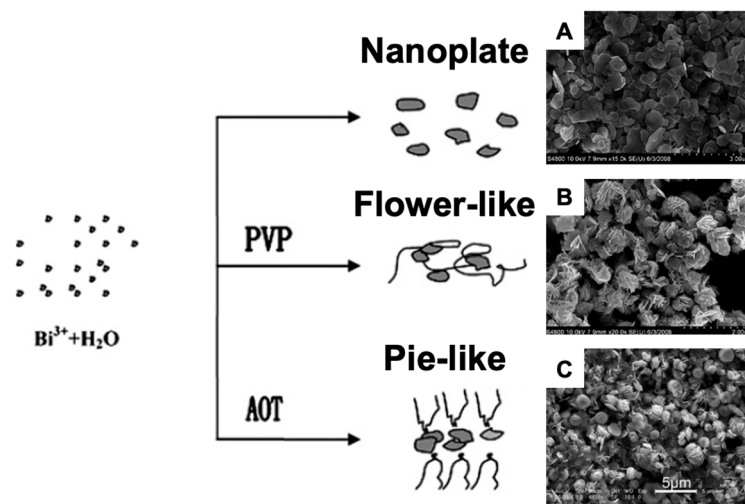


Figure 1. SEM images of BiOCl nanoplate (A), flower-like (B), and pie-like (C) microspheres, as well as the possible growth mechanism. Reproduced with permission from Ref. [36], 2009, Royal Society of Chemistry.

Through a facile hydrothermal route using xylitol as the surfactant, the square-shaped BiOCl nanosheets were synthesized. Through changing the concentration of xylitol, the width of these nanosheets ranged from 50 to 400 nm, and the thicknesses were from 20 to 50 nm, respectively. Meanwhile, the bandgap was narrowed from 3.34 eV to 3.21 eV when the amount of xylitol was 0.1 g, and it had a maximum degradation rate constant of 0.19674 min^{-1} , higher than others [37]. In order to further narrow the bandgap of BiOCl NMs, Zou et al. fabricated a series of hierarchical interconnected BiOCl NMs through the solvothermal method by using a mixture of ethylene glycol-water (1:1, *v/v* ratio) as the

solvent and thiourea as the surfactant [38]. As shown in Figure 2A, the as-prepared BiOCl NMs were nanoplates with thicknesses of ~ 10 nm and diameters of ~ 50 nm with smooth surfaces. When the amount of thiourea was adjusted from 5 to 30 mL, BiOCl microspheres with uniform sizes were formed via the self-assembly process, and the size increased from 400 to 600 nm with increasing amounts of thiourea. Compared with the BiOCl nanoplate, the specific surface area increased from 4.89 to 43.9 $\text{m}^2 \text{g}^{-1}$, and the bandgap was narrowed from 3.11 to 2.22 eV as measured by UV-vis diffuse reflectance spectra (DRS) (Figure 2B). Therefore, BiOCl microspheres have an excellent photocatalytic performance under visible light irradiation against RhB (Figure 2C). Moreover, other solvents or surfactants, such as triethylene glycol [39], ethanol [40], urea [41], mannitol [42], and citric acid [43], were also used to improve the photocatalytic efficacy through regulating their morphologies, as well as their specific surface areas or bandgaps.

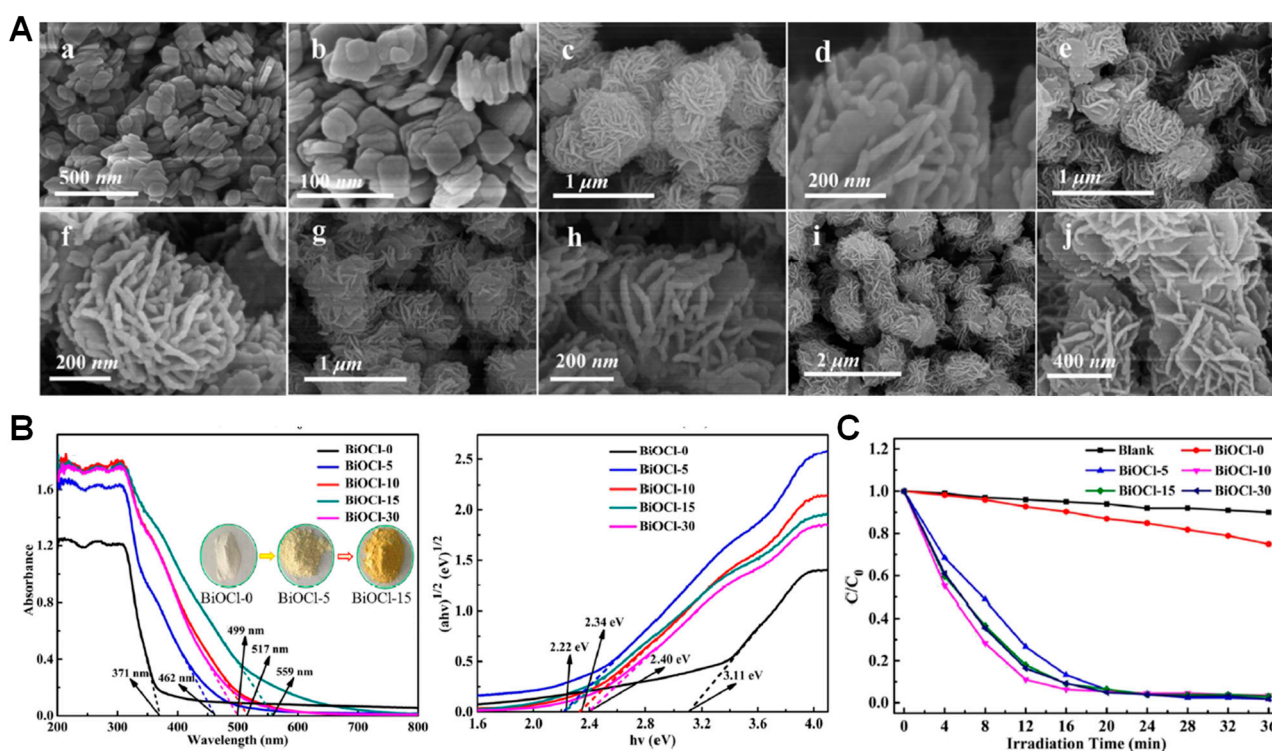


Figure 2. SEM images (A), UV-vis DRS (B), and photocatalytic dye degradation ability (C) of BiOCl NMs synthesized with different amounts of thiourea. For SEM images, BiOCl-0 (a,b), BiOCl-5 (c,d), BiOCl-10 (e,f), BiOCl-15 (g,h), BiOCl-30 (i,j). Reproduced with permission from Ref. [38], 2019, American Chemical Society.

In addition, the morphologies of BiOCl NMs could also be regulated without surfactants. For instance, Wang's and Hao's group successfully fabricated BiOCl flake and nanowire arrays through employing the anodic aluminum oxide (AAO) template assisted sol-gel method. As shown in SEM images (Figure 3A,B), the flakes with a diameter of ~ 3 μm and a thickness of ~ 300 nm were formed perpendicular to the AAO template at a lower concentration of sol, while the nanowires with a diameter of ~ 100 nm and a length ~ 3 μm were growth on the AAO template. For comparison, when the glass template was used, the flake-like film with diameters ranging from 0.5 to 1.5 μm and thicknesses from 50 to 100 nm were formed (Figure 3C). Both the flake and nanowire arrays on the AAO template had stronger adsorption capacity and more effective photocatalytic ability against RhB than the flake-like film on the glass template [44,45]. Moreover, the morphologies and band structures were also regulated by changing the amount of HCl through a simple one-step solvothermal method [46]. As shown in Figure 3D, when the added amount of HCl was less than 4 mmol, the nanoneedle-assembled microspheres were formed. With

increasing amounts of HCl, the nanosheet-assembled microspheres were formed, and the distance between BiOCl nanosheets increased with increasing HCl concentration. The dye degradation experiments showed that nanosheet-assembled microspheres had a higher photocatalytic efficacy than nanoneedle-assembled ones, due to their larger specific surface areas and the stronger reduction capability of photoinduced electrons. BiOCl hollow spheres were also prepared due to the large surface-to-volume ratio and short transport length of mass or charge of the hollow structure [43,47–49]. For example, by using carbonaceous microspheres as sacrificial templates, Yu et. a. obtained BiOCl hollow nanospheres with diameter of ~200 nm and an average shell thickness of 40 nm, which showed high visible light photocatalytic activity towards the degradation of RhB [47].

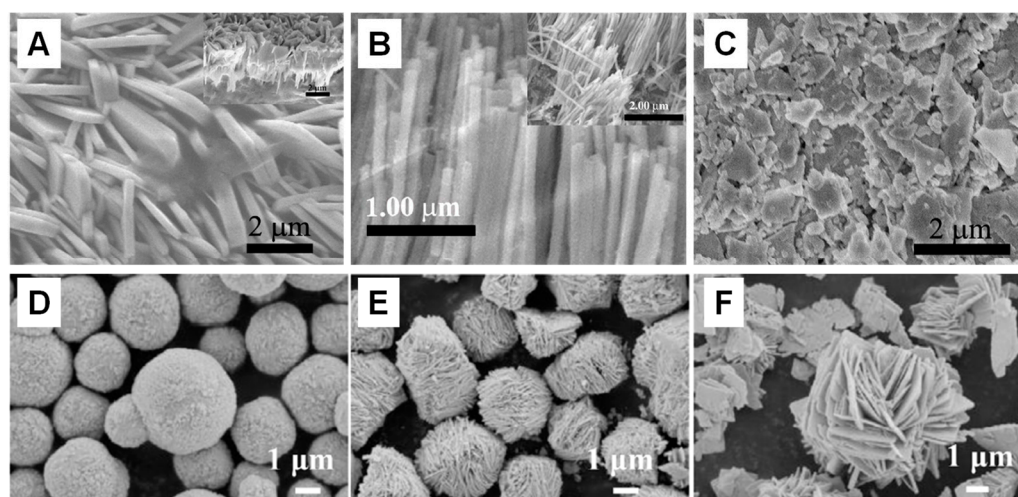


Figure 3. (A–C) SEM images of BiOCl flake (A) and nanowire arrays (B) on AAO template (A), flake-like film on glass template (C); reproduced with permission from Ref. [45], 2010 and 2011, Elsevier (Amsterdam, Netherlands); (D–F) SEM images of BiOCl nanoneedle- and nanosheet-assembled microspheres. Reproduced with permission from Ref. [46], 2020, Elsevier.

2.2. Improved Photodegradation Efficacy through Forming Heterostructures

Semiconductor heterostructures show better photocatalytic performance than pure semiconductors. Table 1 summarizes some BiOCl-based heterostructures and their photocatalytic degradation performance. Facet heterostructures have shown excellent photocatalytic performance, such as the $\text{TiO}_2\{101\}$ - $\text{TiO}_2\{001\}$ heterostructure, which exhibits higher electron-hole spatial separation ability and antibacterial activity than $\text{TiO}_2\{101\}$ or $\text{TiO}_2\{001\}$ nanocrystals [50]. Based on this heterostructure, Zhu's group [51] synthesized BiOCl facet heterostructures and investigated their photocatalytic activities. Through the hydrolysis method under strong acid environment, two different BiOCl nanoplates with different proportions of exposed $\{001\}/\{110\}$ were synthesized. Surface photo-voltage spectra and electrochemistry impedance spectra improved the BiOCl nanoplates, with a lower proportion of $\{001\}/\{110\}$ exhibiting higher electron-hole separation ability. The above two heterostructures could effectively degrade RhB with simulated sunlight irradiation due to the formation of Z-scheme heterostructure, as proved by density functional theory calculation. Due to the similar layer structures of BiOX, BiOCl-BiOX heterostructures have been fabricated. Fan et al. fabricated BiOI $\{001\}$ /BiOCl $\{001\}$ and BiOI $\{001\}$ /BiOCl $\{010\}$ type II heterostructures, in which BiOI $\{001\}$ /BiOCl $\{010\}$ have a better photocatalytic performance because of the shorter photogenerated electron diffusion distance induced by the self-induced internal electric fields of the BiOCl slabs [34]. Meanwhile, BiOCl/BiOBr heterostructures were also designed, which showed excellent photocatalytic degradation performance against organic pollutants (MO and phenol) and pharmaceuticals (levofloxacin and ofloxacin) [52,53].

Table 1. BiOCl-based heterostructures for improving photocatalytic degradation performance.

Heterostructures	Types of Heterostructures	Excited Light	Degradation Performances	Ref.
BiOCl{001}-BiOCl{110}	Z-scheme	150 W Xe lamp without UV cutoff filter	RhB, 50 min, ~100%	[51]
BiOI{001}-BiOCl{010}	Type II	300 W metal-halide lamp with a 420 nm cutoff filter	MO, 3 h, 95%	[34]
BiOCl-BiOBr-Bi ₂₄ O ₃₁ Br ₁₀	Type II	400 W halogen lamp without UV cutoff filter	Levofloxacin, 180 min, 82% Ofloxacin, 180 min, 78.3% Norfloxacin, 180 min, 65.5% Ciprofloxacin, 180 min, 43.4%	[52]
BiOCl-BiOBr	Type II	Visible light (>420 nm)	MO, 40 min, ~95% Phenol, 4 h, ~100%	[53]
BiOCl-TiO ₂	Type II	300 W Xe lamp with a 450 nm cutoff filter	Phenol, 6 h, 43%	[18]
BiOCl-CQDs-ZnIn ₂ S ₄	Type II	300 W Xe lamp with a 420 nm cutoff filter	Tetracycline, 60 min, 82.3% Ciprofloxacin, 90 min, ~80%	[17]
BiOCl-CuO	Type II	150 W infrared lamp (<700 nm)	Oxytetracycline, 90 min, ~70%	[21]
BiOCl-NaBiO ₃	Type II	600 W Xe lamp	Bisphenol A, 60 min, 98.42%	[54]
BiOCl-BiPO ₄	Type II	500 W Xe lamp	RhB, 60 min, 100%	[55]
BiOCl-BiVO ₄	Type II	500 W Xe lamp with a 400 nm cutoff filter	MO, 14 min, 98%	[56]
BiOCl-PbBiO ₂ Cl	Type I	500 W Xe lamp with a 400 nm cutoff filter	MO, 11 h, ~90%	[57]
BiOCl-C ₃ N ₄	Z-scheme	150 W Xe arc lamp	Crystal violet, 12 h, 99%	[58]
BiOCl-K ⁺ Ca ₂ Nb ₃ O ₁₀ ⁻	Z-scheme	300 W Xe lamp	Tetracycline, 60 min, 97.1%	[20]
BiOCl-VO-BiPO ₄	Z-scheme	250 E Xe lamp	Tetracycline hydrochloride, 150 min, 100%	[59]
BiOCl-Au-CdS	Z-scheme	300 W Xe lamp	Carbamazepine, 30 min, 81.7%	[60]
		300 W Xe lamp with an AM 1.5 cutoff filter	MO, 180 min, 100% RhB, 30 min, 100% Phenol, 100 min, 100% Sulfadiazine, 4 h, 100%	

Other heterostructures, including type I, type II, and Z-scheme, have also been designed for improving the degradation efficacy. For type I heterostructures, BiOCl-PbBiO₂Cl heterostructures (Figure 4A) were designed for degrading crystal violet and 2-hydroxybenzoic acid under visible light illumination. Due to the separation of the photo-generated electrons and holes, the reaction rate constant of PbBiO₂Cl/BiOCl h was 3.01 and 2.12 times higher than that of PbBiO₂Cl and BiOCl alone. For type II heterostructures, various NMs, such as TiO₂, BiPO₄, BiVO₄, CuO, and NaBiO₃, were used to form BiOCl-based type II heterostructures. For example, Yu et al. fabricated a BiOCl-NaBiO₃ heterostructure by using NaBiO₃ and hydrochloric acid aqueous solutions as the raw materials [54]. This heterostructure shows higher photodegradation efficacy due to the excellent electron and hole separation abilities (Figure 4B). BiPO₄ NMs with different amounts were also incorporated on BiOCl NMs (Figure 4C), in which a 40% BiPO₄-BiOCl composite could degrade 98% of MO within only 14 min under simulated sunlight irradiation because of the formation of a p-n junction [55]. A similar BiOCl-BiVO₄ p-n junction has also been reported by Song's group [56]. Compared with type I and type II heterostructures, Z-scheme heterostructures could not only separate photogenerated electrons and holes effectively, but also keep their strong redox abilities. Several BiOCl-based Z-scheme heterostructures were designed to improve their photocatalytic performance. Au was a commonly used mediator to form semiconductors in Z-scheme heterostructures. Zhang et al. introduced Au to form a BiOCl-Au-CdS indirect Z-scheme heterostructure (Figure 4D), which could degrade the anionic dye MO, the cationic dye RhB, phenol, and the antibiotic sulfadiazine with simulated sunlight irradiation [60]. Oxygen vacancy (OV) was also used to form a BiOCl-OV-BiPO₄ direct Z-scheme heterostructure, in which oxygen vacancy acted as an electron mediator in the Z-scheme to promote the separation efficiency of photogenerated

electron–hole pairs with high redox ability (Figure 4E) [59]. In addition, a BiOCl-based direct Z-scheme heterostructure, such as BiOCl-C₃N₄ and BiOCl-K⁺Ca₂Nb₃O₁₀⁻, were also fabricated for RhB and tetracycline hydrochloride degradation [20]. Therefore, tuning morphologies and forming heterostructures could enhance the photocatalytic degradation efficacy of BiOCl NMs.

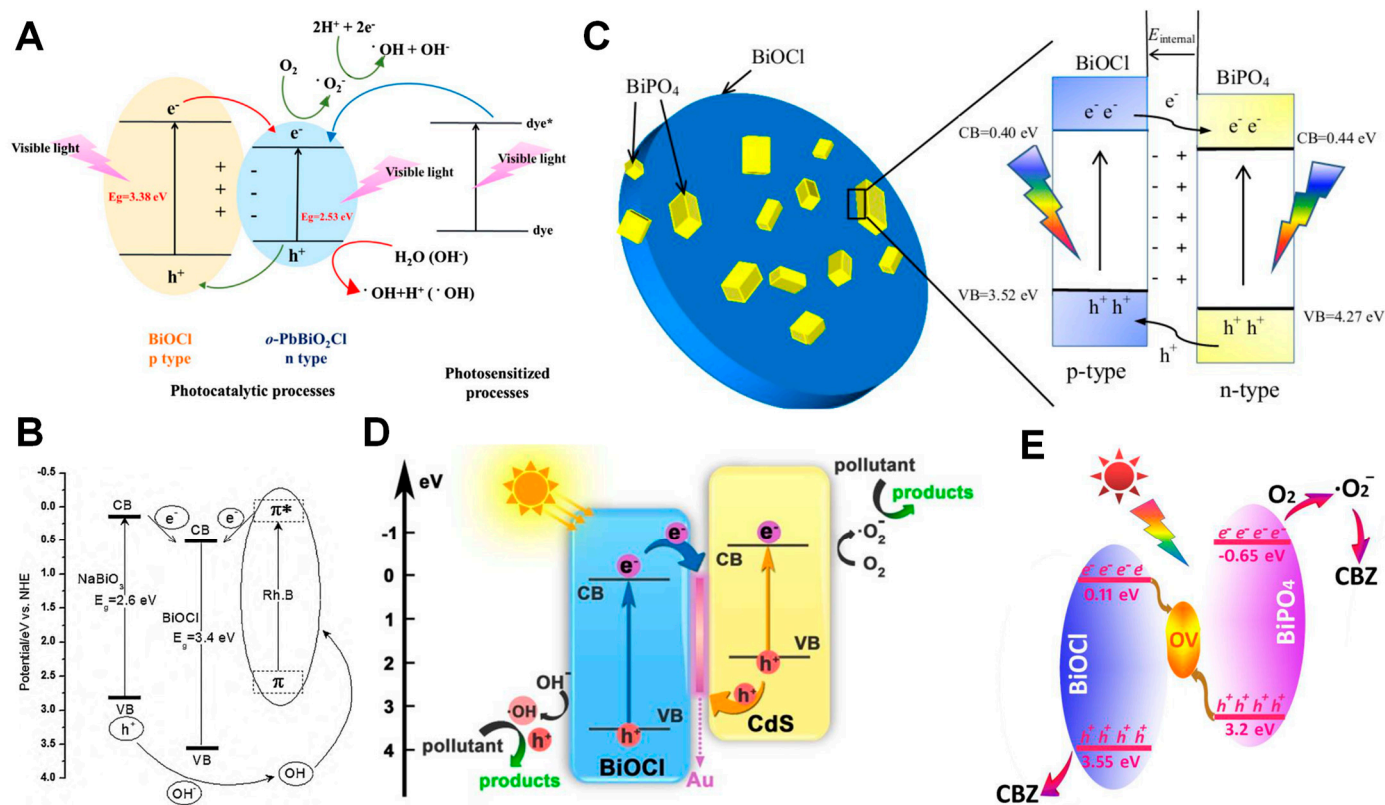


Figure 4. Scheme of various BiOCl-based heterostructures. (A) BiOCl-PbBiO₂Cl type I heterostructure. Reproduced with permission from Ref. [57], 2018, Elsevier. (B) BiOCl-NaBiO₃ type II heterostructure. Reproduced with permission from Ref. [54], 2010, Elsevier. (C) BiOCl-BiPO₄ type II heterostructure. Reproduced with permission from Ref. [55], 2016, Elsevier. (D) BiOCl-Au-CdS Z-scheme heterostructure. Reproduced with permission from Ref. [60], 2017, American Chemical Society. (E) BiOCl-OV-BiPO₄ Z-scheme heterostructure. Reproduced with permission from Ref. [59], 2018, Elsevier.

3. BiOCl NMs Used as Theranostic Platform

Since the late 19th century, bismuth subsalicylate has been used to relieve nausea, diarrhea, and gastrointestinal discomfort. It can be hydrolyzed into BiOCl in the human body to effectively treat diarrhea and upset stomach [61,62], proving the excellent biocompatibility of BiOCl NMs. Recently, BiOCl NMs have been used as a theranostic platform, including for drug delivery [63], bioimaging [64–66], biosensors, Alzheimer’s disease [67], antibacterial, and anticancer applications [68,69].

3.1. Bioimaging

Bismuth-based NM has been used as an ideal X-ray computed tomography (CT) contrast agent due to the higher atomic numbers and X-ray attenuation coefficient of Bi elements [24]. As a typical Bismuth-based NM, BiOX NMs, such as BiOI [70], BiOBr [71], and BiOCl, have recently been used for spatial- and temporal-specific CT imaging of tumors. However, only a few studies on bioimaging of BiOCl NMs have been reported. As reported by Ye’s group [64], Se-doped BiOCl nanosheets were fabricated via a solvothermal method. As shown in the top and cross-sectional views of the mouse (Figure 5A), the evident signal-

to-noise ratio changes from 39.24 to 82.12 at 1 h post-injection, meaning the excellent X-ray CT imaging ability of Se-doped BiOCl nanosheets. Multimodal imaging that integrates several imaging technologies, such as fluorescence imaging, magnetic resonance imaging, and photoacoustic (PA) imaging, can diagnose tumors more precisely and quickly. In order to obtain BiOCl NMs with multi-mode diagnostic ability, Zhang's and Wang's groups introduced oxygen vacancies into BiOCl NMs. As shown in Figure 5B, with increasing Bi concentrations, significantly enhanced hounsfield unit (HU) values were observed in oxygen-vacancy-rich BiOCl containing aqueous solution. Meanwhile, in vivo CT imaging on tumor-bearing mice showed (Figure 5C) that the HU values on tumors enhanced from 71.6 to 113.3, proving the good CT imaging ability. Moreover, after introducing oxygen defects, PA signals were observed. In order to investigate the relationship between PA signals and oxygen defects, three O-BiOCl nanosheets with different oxygen defects were fabricated. As shown in Figure 5D, with an increasing amount of oxygen defects, PA signals enhanced about 2.0 and 5.5 times, respectively. After intratumoral injection of oxygen-vacancy-rich BiOCl nanosheets into 4T1 tumor-bearing mice, Figure 5E showed that the PA value increased from 0.135 to 0.636, proving the excellent CT and PA imaging ability. In addition, oxygen-vacancy-rich BiOCl s have also been used for PA imaging for Panc-1 tumors through intravenous injection, as shown in Figure 5F [66].

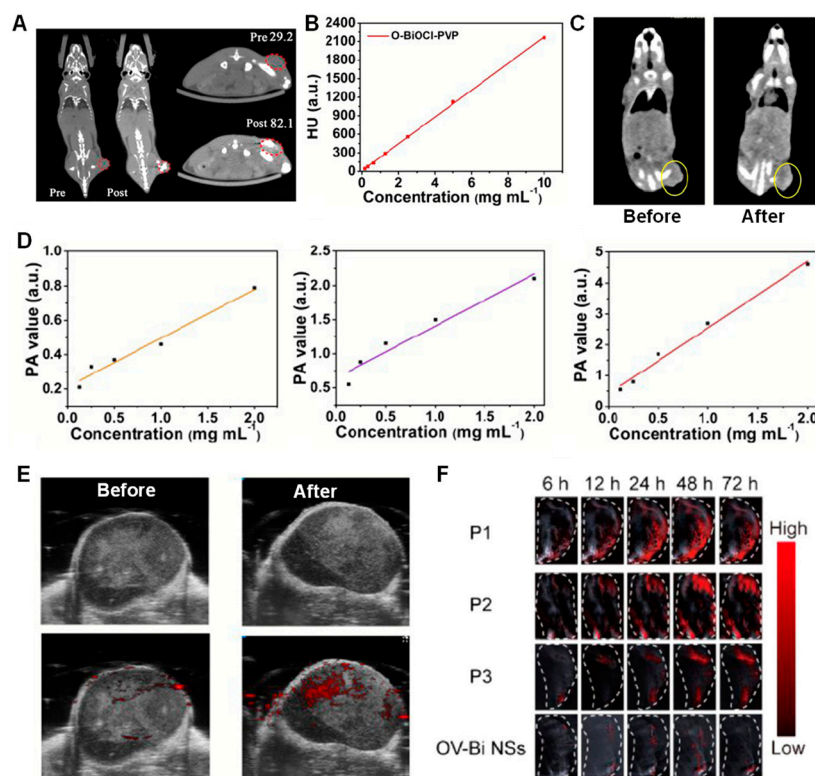


Figure 5. CT and PA imaging abilities of BiOCl NMs. (A) The CT images of front view and side view with and without injected Se-doped BiOCl. Reproduced with permission from Ref. [64], 2019, American Chemical Society; (B,C) in vitro and in vivo CT imaging ability of oxygen-vacancy-rich BiOCl; (D) PA signals of OBP-1, OBP-2, and OBP-3; (E) PA imaging of 4T1 tumor-bearing mice before and after intratumoral injection of oxygen-vacancy-rich BiOCl. Reproduced with permission from Ref. [65], 2020, Royal Society of Chemistry. (F) PA imaging of Panc-1 tumor-bearing mice before and after intravenous injection of oxygen-vacancy-rich BiOCl. Reproduced with permission from Ref. [66], 2021, Elsevier.

3.2. Biosensor

The release of pesticide residue and antibiotics has become a public health concern. Therefore, the detection of biomarkers, pesticides, and antibiotics has a significant impact

on human health. Photoelectrochemical sensing is becoming an innovative technique due to its simple detection equipment, rapid analysis, and high sensitivity abilities [72]. As shown in Table 2, a series of BiOCl-based NMs have been developed to detect various substances, such as pesticides, antibiotics, and biomarkers, due to the faster separation efficiency of photogenerated carriers. Antibiotics, such as ciprofloxacin, chloramphenicol, kanamycin, and lincomycin, have been widely used for the treatment of bacterial infections and showed good therapeutic effects. However, they cannot be fully absorbed and degraded, leading to environmental and water pollution, or even worse to adverse effects on the health of humans. For instance, the release of ciprofloxacin has caused serious threats to human health. Yuan's group [73,74] first designed a BiOCl-based PEC sensor for the detection of ciprofloxacin through monitoring the changes of photocurrents produced by BiOCl under irradiation. In order to improve the sensitivity of the BiOCl-based PEC sensor, graphitic carbon nitride or metallic Bi were used to form heterostructures with BiOCl NMs to separate photogenerated carriers. Both of these heterostructures show much higher photocurrents than BiOCl alone, thus leading to higher detection ranges and limits. In order to obtain a PEC sensor with high selectivity, the aptamer, which serves as a specific biometric molecule due to its biological affinity and specific recognition with a specific analyte, was usually decorated on the surface to form PEC aptasensor. Li et al. [75] designed an aptamer-modified BiOCl-Bi₂₄O₃₁Cl₁₀ PEC aptasensor, which can be applied to the determination of ciprofloxacin in water with good selectivity and reproducibility. The residues and metabolites of chloramphenicol also cause damage to the human hematopoietic and gastrointestinal system. Li's group [76] designed Ag nanoparticles modified with a BiOCl NM (BiOCl-Ag) PEC aptasensor, which could effectively improve the absorption of incident light and promote the migration and separation of photogenerated carriers due to the surface plasmon resonance (SPR) of Ag NMs. After decorating with the aptamer, there were obvious changes to the photocurrent when incubating the BiOCl-Ag PEC aptasensor with chloramphenicol, while no changes were observed in the other subjects, such as tetracycline, lincomycin, oxytetracycline, bisphenol A, norfloxacin, and hexafluorobisphenol A, proving the good selectivity due to the specific binding of the chloramphenicol-aptamer. In addition, other antibiotics, such as kanamycin and lincomycin, were also detected by the BiOCl-MnO₂ and BiOCl-Au-CdS heterostructure PEC aptasensor, with excellent sensitivity and selectivity, respectively [77,78].

Table 2. BiOCl-based NMs used as photoelectrochemical sensing platform.

Substance	BiOCl-Based NMs	Detecting Subject	Detection Range	Detection Limit	Refs.
Antibiotics	BiOCl-Bi	ciprofloxacin	0.16~9.64 $\mu\text{g mL}^{-1}$	0.05 $\mu\text{g mL}^{-1}$	[73]
	BiOCl-C ₃ N ₄	ciprofloxacin	0.5~1840 ng mL^{-1}	0.2 ng mL^{-1}	[74]
	BiOCl-Bi ₂₄ O ₃₁ Cl ₁₀	ciprofloxacin	5.0~1.0 $\times 10^4 \text{ ng mL}^{-1}$	1.67 ng mL^{-1}	[75]
	BiOCl-Ag	chloramphenicol	0.2~1.0 $\times 10^4 \text{ pM}$	0.08 pM	[76]
	BiOCl-MnO ₂	lincomycin	1.0 $\times 10^{-3}$ ~1.0 $\times 10^3 \text{ nM}$	3.33 $\times 10^{-4} \text{ nM}$	[78]
	BiOCl-Au-CdS	kanamycin	50~5000 fM	29 fM	[77]
Pesticides	BiOCl-Au	4-chlorophenol	0.16~20 mg L^{-1}	0.05 mg L^{-1}	[79]
	BiOCl-BiPO ₄	4-chlorophenol	20~3.38 $\times 10^4 \text{ ng mL}^{-1}$	6.78 ng mL^{-1}	[80]
	BiOCl-GQDs	chlorpyrifos	0.3~80 ng mL^{-1}	0.01 ng mL^{-1}	[81]
	BiOCl-TiO ₂	chlorpyrifos	1~12 μM	0.11 μM	[82]
	BiOCl _{0.5} Br _{0.5} -C ₃ N ₄ -Au	2-chloroethyl phosphate	20~6.3 $\times 10^4 \text{ nM}$	6.9 nM	[83]
Antibiotics	BiOCl-graphene	glucose	0.5~10 mM	0.22 mM	[84]
	BiOCl-TiO ₂	glucose	0~1300 μM	5.7 μM	[85]
	BiOCl	glutathione	0.01~20 μM	0.6 μM	[86]
	BiOCl-BiPO ₄ -CDs	dopamine	1~1.0 $\times 10^4 \text{ pM}$	0.3 pM	[87]
	BiOCl-Bi ₂ S ₃ -CdS	alkaline phosphatase	0.1~4000 U L^{-1}	0.06 U L^{-1}	[88]
	BiOCl-C ₃ N ₄	carcinoembryonic antigen	0.1~1.0 $\times 10^4 \text{ pg mL}^{-1}$	0.1 pg mL^{-1}	[89]
	BiOCl-CdS	carcinoembryonic antigen	0.01~40.0 ng mL^{-1}	0.002 ng mL^{-1}	[90]

Table 2. Cont.

Substance	BiOCl-Based NMs	Detecting Subject	Detection Range	Detection Limit	Refs.
Others	BiOCl-CuO	aflatoxin B1	$0.5\sim 1.0 \times 10^5 \text{ pg mL}^{-1}$	0.07 pg mL^{-1}	[91]
	BiOCl	Pb ions	$0.2\sim 300 \text{ }\mu\text{g L}^{-1}$	33 ng L^{-1}	[92]
	BiOCl-CuS-FeN ₃	naproxen	$0.2\sim 500 \text{ }\mu\text{M}$	$0.06 \text{ }\mu\text{M}$	[93]

Pesticides, which are widely used in agriculture, also cause serious pollution of the environment and threaten the health of human beings. It has been reported that serious symptoms of the nervous system, such as dizziness, rash, and itching could be caused through drinking 4-chlorophenol-contaminated water for a long time [94]. A BiPO₄-BiOCl heterostructure PEC aptasensor has been designed for detecting 4-chlorophenol in wastewater samples [80]. The photoelectrochemical characterization implied that the BiOCl-BiPO₄ heterostructure could induce the highest photocurrent, compared with BiOCl or BiPO₄ alone, leading to a wider linear range and a lower detection limit of 4-chlorophenol. Further real sample analysis (wastewater samples from Yudai River at Jiangsu University) by a PEC aptasensor shows a similar result measured by high-performance liquid chromatography (HPLC). Zhang's group has also obtained a BiOCl-Au PEC aptasensor, the detection range and limit of which were determined to be $0.16\sim 20 \text{ mg L}^{-1}$ and 0.05 mg L^{-1} , respectively [79]. Moreover, this PEC aptasensor shows the negligible interference of 4-chlorophenol detection when adding metal ions or dyes into 4-chlorophenol aqueous solutions, indicating it can be used for real sample detection rather than experimental samples. Chlorpyrifos, as one type of broad-spectrum organophosphorus pesticide, also endangers the health of humans and animals. Through the one-pot precipitation method, a Z-scheme iodine-doped BiOCl (I-BiOCl)-nitrogen-doped graphene quantum dot (N-GQDs) heterostructure was fabricated, in which iodine doping could narrow the bandgap of BiOCl, and the formed heterostructure could not only absorb more incident light but also separate photogenerated carriers, leading to sensitivity of the detection range and limit [81]. Based on the sensitivity of the BiOCl heterostructure PEC aptasensor, Tan's group [82] detected doses of chlorpyrifos on lettuce, leek, and cucumber with a BiOCl TiO₂ PEC aptasensor, which also proves that a BiOCl-based PEC aptasensor could be applied for analysis of real samples. 2-chloroethyl phosphate, as a rapid ripening agent for fruits and vegetables, has been a concern regarding food security issues. Juan et al. prepared a bismuth oxychloride/bismuth oxybromide (BiOCl_{0.5}Br_{0.5})-C₃N₄-Au heterostructure PEC aptasensor, which has a detection limit of 6.9 nM 2-chloroethyl phosphate and been used for tomato samples [83]. Aflatoxin B1, known as a class of secondary fungal metabolites, could induce serious illnesses to humans and animals even at an extremely low dose. Thus, a BiOCl-CuO PEC aptasensor with ultra-sensitivity (0.07 pg mL^{-1}) was designed by Zhang's group. More importantly, this aptasensor could also degrade aflatoxin B1 under light irradiation and suitable bias voltage, and the degradation rate could reach up to ~81.3% when $5.0 \text{ }\mu\text{g mL}^{-1}$ of aflatoxin B1 was added [91].

In addition to bioimaging, the detection of biomarkers, such as glucose, glutathione (GSH), dopamine, alkaline phosphatase (ALP), and tumor markers, is a widely used method to diagnose various diseases. Among these biomarkers, glucose is a common biomarker, whose concentration is critically significant in many facets of biological research and medical specialties. Enzyme-based electrochemical biosensors have been widely used due to its good selectivity and sensitivity. In order to solve the limitations of enzyme-based electrochemical biosensors, such as complicated enzyme immobilization procedures, instability, restricted operational conditions, and poor reproducibility, BiOCl-graphene and BiOCl-TiO₂ heterostructures were designed and prepared for glucose detection, and the detection limit was 0.22 mM and 5.7 μM , respectively [84,85]. The changes of ALP also reflect numerous illnesses, such as hepatitis, diabetes, bone disease, and prostate cancer. Luo et al. [88] designed a BiOCl-Bi₂S₃-CdS Z-scheme heterostructure for PEC detection of ALP with a limit of 0.06 U L^{-1} . Moreover, in order to detect human serum

samples, the selectivity of ALP and stability in blood of this sensor were investigated. Compared with the interfering substances, including egg albumin, GSH, L-cys, GOx, DA, Na⁺, K⁺, BSA, and UA, ALP could be specifically measured. Meanwhile, during 10 on/off cycles, the photocurrent induced by this sensor did not obviously change. The result implies the potential and preliminary application of BiOCl-Bi₂S₃-CdS Z-scheme PEC biosensors in actual sample analysis. Meanwhile, GSH and dopamine were also detected by a BiOCl-based PEC biosensor [86,87]. Tumor markers are usually detected through ELISA, chemiluminescent, fluorescent, or colorimetric techniques. The PEC immunoassay has been developed rapidly due to its high sensitivity. Taking a carcinoembryonic antigen (CEA) as an example, after modifying the CEA antibody for selective recognition of the CEA target, the BiOCl-based PEC immunoassay could effectively detect CEA in serum samples [89,90]. In addition, other substances, such as Pb ions [92] and naproxen [93], were also detected by various BiOCl-based PEC sensors.

3.3. Antibacterial

One of the serious threats to the world's public health is bacterial invasion, which could induce cholera, pneumonia, influenza, tuberculosis, measles, meningitis, etc. Therefore, bacteria inactivation is significant. However, traditional antibiotics bring bacterial resistance, and moreover, the antibiotic itself is toxic to animals and humans. Due to the capability of ROS generation, there were some studies on the photocatalytic antibacterial abilities of BiOCl-based NMs. In fact, BiOCl NMs hydrolyzed by bismuth subsalicylate have been reported to act upon enteric pathogens without light irradiation in the gastrointestinal tract [61]. In order to study the mechanism of the antimicrobial properties of bismuth subsalicylate [95], Jan et al. investigated the antimicrobial effects of bismuth subsalicylate and BiOCl on *Clostridium difficile*, *Salmonella*, *Shigella*, Shiga toxin-producing *Escherichia coli* strains, and norovirus. The results indicated that bismuth subsalicylate and BiOCl have similar antimicrobial effects on a wide range of diarrhea-causing pathogens. Inspired by the excellent ROS generation ability, BiOCl-based NMs have been used to kill both Gram-positive and Gram-negative bacteria, including *Staphylococcus aureus*, *Enterococcus faecalis*, *Escherichia coli*, and *Pseudomonas aeruginosa* [96]. To enhance antibacterial efficacy, Ag nanoparticles are usually used to couple with BiOCl NMs [97,98]. On the one hand, Ag could not only enhance the light absorption ability due to the SPR effect, but also separate photoinduced electrons and holes as a result of heterostructure; on the other hand, Ag nanoparticles could release Ag⁺, which could kill bacteria effectively [99]. Forming a semiconductor heterostructure could also improve antibacterial efficacy. For example, BiOCl-AgCl [100], BiOCl-Bi₃O₄Cl [101], and BiOCl-BiO_{1.84}H_{0.08} [102] heterostructures were designed, and showed that effective visible light triggered antibacterial performance. The binding between bacteria and antibacterial agents is another important key to improving the efficacy of bacterial inactivation. In order to regulate the binding ability with bacteria, Yu's group [103] used PEG (M_w = 10000) and cetrimonium bromide (CTAB) as a template to prepare two vacancy types of BiOCl microspheres (Figure 6A). Fourier transform infrared spectroscopy showed no peaks of these two templates, which ruled out the effect of templates on the following bioeffects of the microspheres. The positron lifetime spectra and zeta potential proved that PEG-modified BiOCl microspheres exhibited one negative charge (−1.58 mV), while CTAB-modified BiOCl microspheres possessed ten negative charges (−15.95 mV). As shown in Figure 6B, the adsorption ability of BiOCl microspheres to the bacterial cell wall components liposaccharide (LPS, for Gram-negative bacteria) and teichoic acid (TA, for Gram-positive bacteria) were further investigated via first-principles computations, which proved that PEG-modified BiOCl showed a higher capacity to adsorb both LPS and TA than CTAB-modified BiOCl. Additionally, the adsorption experiments also showed that PEG-modified BiOCl adsorbed 68% of LPS and 56% of TA, while CTAB-modified BiOCl only adsorbed 21% of LPS and 28% of TA. Therefore, PEG modified BiOCl has a much higher binding ability to both Gram-negative and Gram-positive bacteria than CTAB-modified BiOCl, thus could effectively kill bacteria.

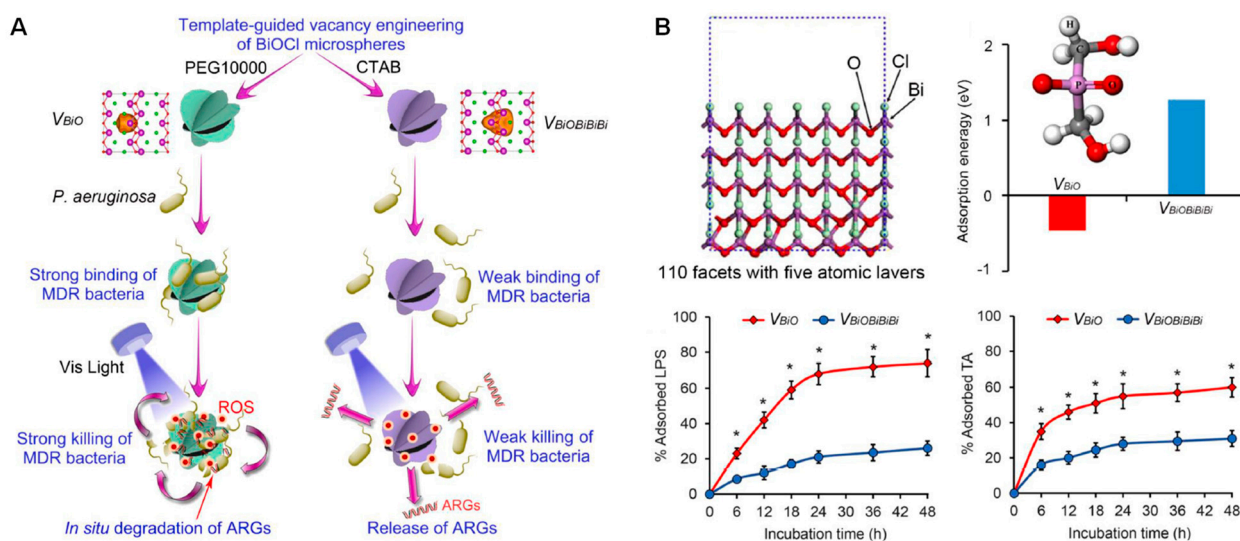


Figure 6. (A) Scheme of vacancy engineering of BiOCl microspheres for binding and killing bacteria; (B) Adsorption ability of the BiOCl microspheres to bacterial cell wall components LPS and TA via first-principles computations and experiments. * indicates significant difference between the two groups at the indicated time point ($p < 0.05$). Reproduced with permission from Ref. [103], 2021, Elsevier.

Inspired by the excellent antibacterial activity, our group [104] designed Bi_2Te_3 -functionalized BiOCl (BOBT) for enhancing antibacterial activity and wound healing efficacy with sunlight irradiation (Figure 7). The bandgap of BiOCl was narrowed from 3.25 eV to 2.37 eV, as proved by UV diffuse reflectance spectroscopy. With simulated sunlight irradiation, BOBT could effectively produce ROS and inhibit the growth of both Gram-positive and Gram-negative bacteria. In vivo experiments further confirmed the excellent wound healing capability of BOBT.

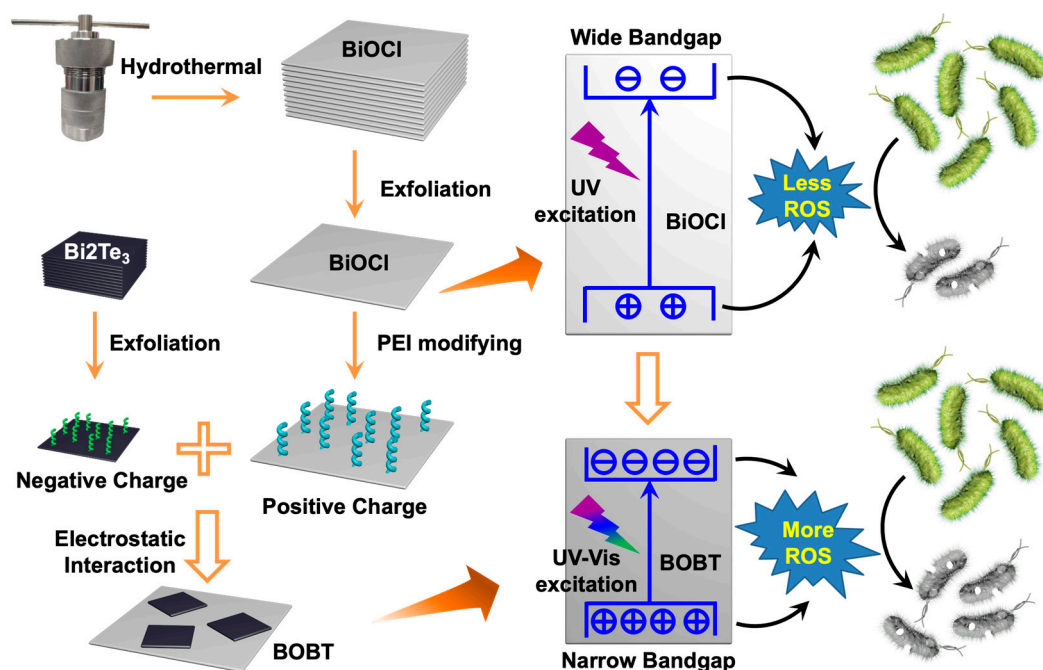


Figure 7. Antibacterial activity of Bi_2Te_3 -functionalized BiOCl NMs. Reproduced with permission from Ref. [104], 2021, Royal Society of Chemistry.

3.4. Anticancer

The incidence rate and mortality rate of cancer are increasing year by year. According to the latest report from the World Health Organization, in 2020 there were 19.29 million new cancer cases and 9.96 million deaths [105]. As a non-invasive treatment technology, some new therapeutic methods based on nanotechnology, such as photodynamic therapy (PDT), photothermal therapy (PTT), and sonodynamic therapy (SDT), are widely used due to their advantages of strong tissue penetration, high efficiency, low side effects, and broad-spectrum anticancer applications. As semiconductors, more and more bismuth-based semiconductor NMs, such as bismuth sulfide [25,26], BiOBr [106], and Cu_3BiS_3 [107], have been used as PDT agents due to their ROS generation capabilities under light irradiation. Based on the excellent photocatalytic activity, Wu et al. first applied layered BiOCl NMs toward cancer PDT [108]. BiOCl nanosheets and nanoplates were synthesized through a hydrothermal method. Both of them have square shapes (Figure 8A) and have ideal dispersion stability after ultrasonic dispersion and polyetherimide (PEI) modification. Compared with the commonly used photocatalyst (P25), both BiOCl nanosheets and nanoplates could effectively degrade methyl violet and kill tumor cells with UV light irradiation (Figure 8B,C). These BiOCl nanosheets could also kill ~20% of MCF-7 cells without light irradiation, indicating that BiOCl nanosheets are slightly toxic to cells. However, the above BiOCl NMs could only be excited by UV light due to their wide bandgaps, which limited their applications to only cancer cells due to the side effect of UV light. Therefore, Se-doped BiOCl were synthesized to narrow the bandgap by Ye's group [64]. After doping, the absorption had a redshift from 387 nm of BiOCl to 540 nm of Se-doped BiOCl, which could be irradiated by visible light. As is well known, both UV and visible light have weaker tissue penetration capabilities than near-infrared (NIR) light. Therefore, Yang's group adjusted the exciting light of BiOCl to NIR through hybridizing with upconversion nanoparticles (UCNPs) [109]. TEM images in Figure 9A show that the smaller UCNPs were distributed on the surface of the BiOCl nanosheet, and the absorption of the BiOCl nanosheet is well matched with the emission of UCNPs (Figure 9B), indicating BiOCl nanosheets could be excited by the emitted light of UCNPs under irradiation. As a result, it could produce ROS with NIR light irradiation (Figure 9C), thus killing tumor cells (Figure 9D) and eliminating tumors (Figure 9E). Meanwhile, they also doped lanthanide into BiOBr NMs to endow them with NIR light-responsive PDT activity [71].

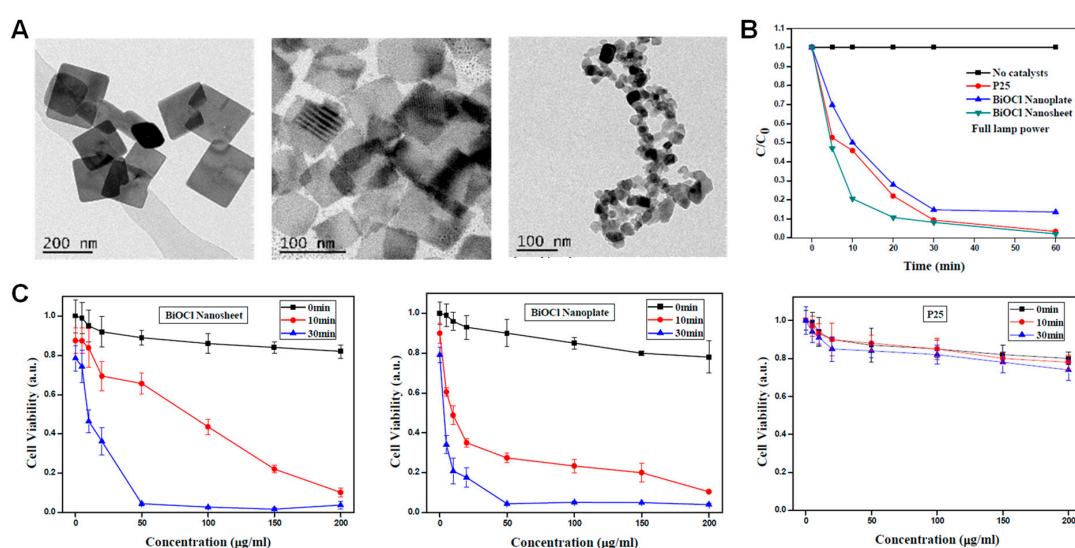


Figure 8. BiOCl NMs used for PDT against cancer cells. (A) TEM images of BiOCl nanosheets, nanoplates and P25 nanoparticles; (B,C) photocatalytic degradation of methyl violet (B) and cell-killing (C) abilities of BiOCl nanosheets, nanoplates, and P25 nanoparticles. Reproduced with permission from Ref. [108], 2016, Royal Society of Chemistry.

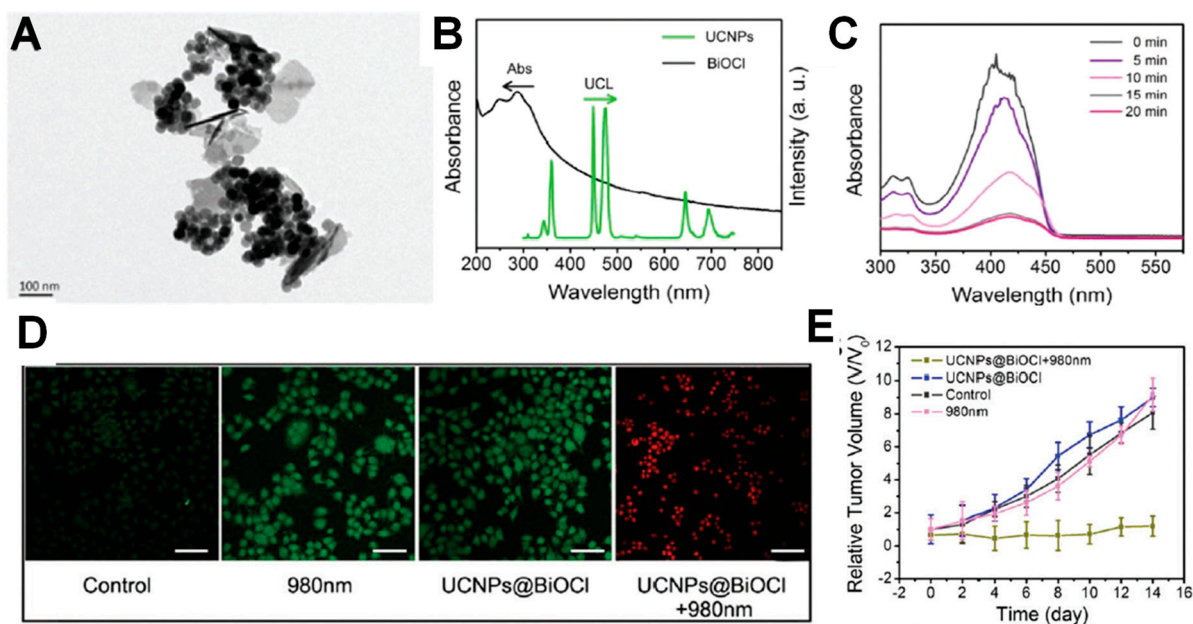


Figure 9. UCNP-BiOCl NMs used for PDT against cancer cells. (A) TEM images of UCNP-BiOCl nanosheets; (B) the emission spectrum of UCNPs and absorption spectrum of BiOCl nanosheet; (C) DPBF absorbance spectrum after treating with UCNP-BiOCl nanosheet with irradiation of 980 nm laser; (D) Dead/live staining of cells treated with UCNP-BiOCl NMs; (E) Tumor growth curves treated with UCNP-BiOCl NMs. Reproduced with permission from Ref. [109]. 2017, Royal Society of Chemistry.

In addition to PDT agents, bismuth-based NMs have also been used as other therapeutic agents, including SDT, PTT, and radiotherapy agents. NIR-activated PTT are a promising technology for tumor ablation. Usually, the photothermal properties are generated from localized surface plasmon resonances or narrow bandgaps (smaller than 1.53 eV) [24,110]. However, photothermal performance has also been observed for semiconductor bandgaps greater than 1.53 eV, the photothermal properties of which may originate from various defects, such as deep level defects in bismuth sulfide [111], hydrogen impurity in TiO₂ [112], and oxygen vacancies in manganese dioxide [113] or bismuth tungstate [114]. Inspired by oxygen-vacancy-induced photothermal performance, oxygen vacancies have been introduced to BiOCl to endow them photothermal properties [65]. As shown in Figure 10, after exposure to UV light, oxygen vacancies could be induced and tuned easily, leading to a strong light absorption in NIR windows, as well as a high photothermal conversion efficiency. The concentration of oxygen vacancies could be tuned by changing the UV irradiation time from 2 to 12 h. After 12 h of exposure to UV light, the maximum temperature and photothermal conversion efficiency of BiOCl could reach up to 65 °C and 13.9%, respectively, higher than that exposed for 2 and 6 h. In addition, UCNPs were also used to form heterostructures with BiOCl to endow them with photodynamic and photothermal performances for tumor therapy under NIR laser irradiation [68].

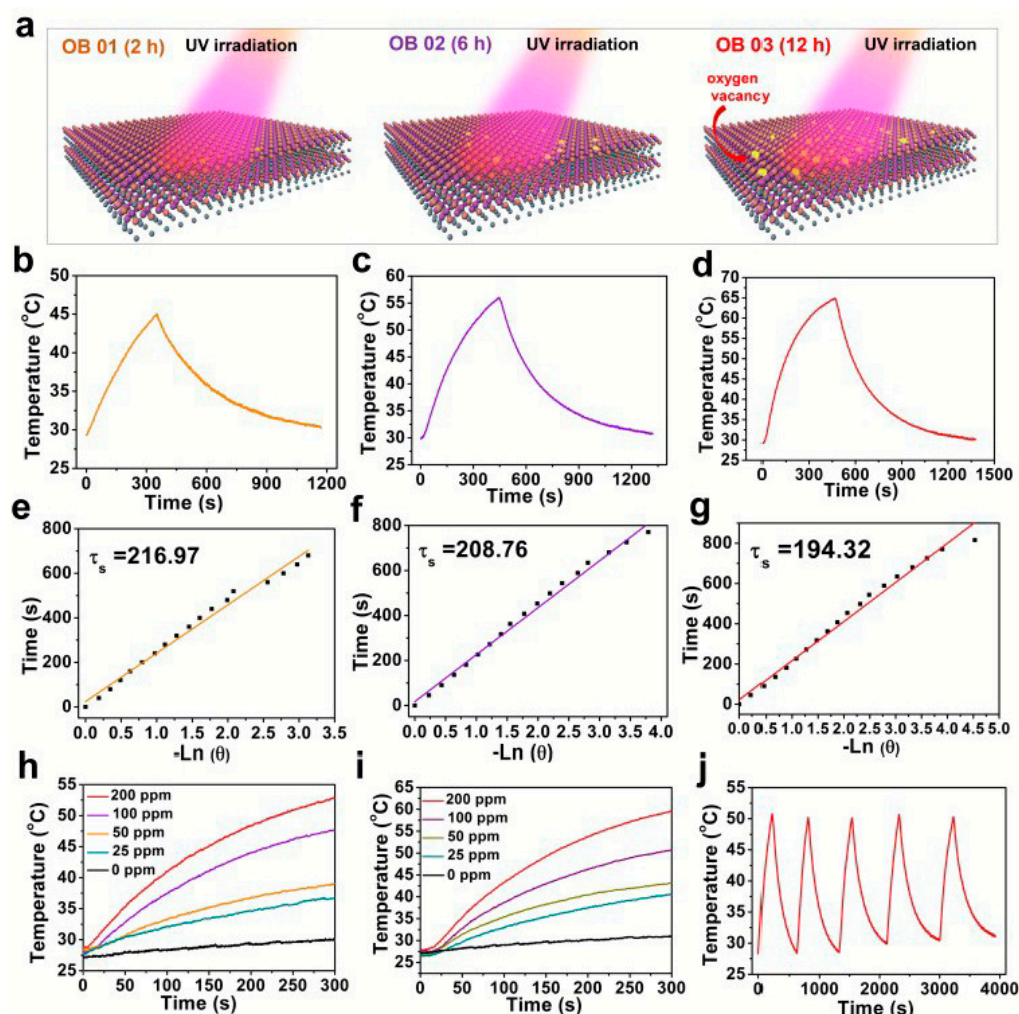


Figure 10. PTT performance of BiOCl induced by oxygen vacancies. Reproduced with permission from Ref. [65], 2020, Royal Society of Chemistry. (a) 3D schematic illustration of BiOCl nanosheets containing different amounts of oxygen vacancies after exposure to UV irradiation for 2, 6 and 12 h. (b–g) Photothermal effect (b–d) and time constant (e–g) of BiOCl nanosheets after the exposure to UV irradiation for 2 (b,e), 6 (h,f), and 12 h (d,g). (h–i) The photothermal-heating curves of BiOCl nanosheets under 808 nm laser irradiation at a power density of 1.5 (h) and 2.0 W cm⁻² (i). (j) Recycling-heating profiles of BiOCl nanosheets aqueous solution after 808 nm laser irradiation at 2.0 W cm⁻² for five laser on/off cycles.

Considering the tissue penetration capability, ultrasound and X-ray are also used for irradiating semiconductors through different mechanisms. With ultrasound irradiation (20 kHz~1 GHz), the microbubbles (cavitation nuclei) existing in the liquid will vibrate, grow, and continuously gather the sound field energy. When the energy reaches the threshold, the cavitation nuclei will collapse and release the energy, producing local high temperature and high pressure (5000 K, 1800 ATM), thus resulting in the decomposition of water molecules and the fracture of chemical bonds. When these broken chemical bonds are recombined, they will release energy and produce luminescence (sonoluminescence). The emitted light is mainly ultraviolet light, which can be used to stimulate most semiconductor materials to generate ROS [115]. Therefore, BiOCl NMs could be excited by ultrasound to produce ROS. Based on this mechanism, Wang et al. [66] designed oxygen-vacancy-rich BiOCl nanosheets modified with PTP and CRK peptides (Figure 11), in which BiOCl served as the sonosensitizer for ROS generation, oxygen vacancies were introduced to enhance ROS generation and induce PA imaging ability, and PTP and CRK peptides were modified to target cancer cells and mitochondria through plectin-1 and p32 proteins,

respectively. Electron paramagnetic resonance (EPR) spectrum showed that OV-Bi NSs could produce both $^1\text{O}_2$ and $\text{OH}\cdot$ under ultrasound irradiation. Moreover, in vitro and in vivo experiments proved that oxygen-vacancy-rich BiOCl NSs modified with PTP and CRK peptides could effectively enter into cancer cells and target mitochondria, thus leading to cell death and tumor elimination, providing a potent nanomedicine for the diagnosis and treatment of pancreatic cancer. GSH, which was highly expressed in tumor tissues, could reduce ROS to protect cancer cells from oxidative stress injury. Therefore, Zhang's group modified oxygen-vacancy-rich BiOCl NSs with L-buthionine-sulfoximine (BSO), an inhibitor of biosynthesis of GSH, to improve SDT efficacy [69]. With ultrasound irradiation, PEG decorated oxygen-vacancy-rich BiOCl NSs could effectively amplify cellular oxidative stress due to the production of $^1\text{O}_2$ and inhibition of GSH. Further in vitro and in vivo experimental results show good SDT efficacy of BSO-modified oxygen-vacancy-rich BiOCl NSs. In addition, the routine analysis of blood, blood biochemistry, biodistribution, and H&E staining of major organs indicated the excellent biocompatibility of BSO-modified oxygen-vacancy-rich BiOCl NSs.

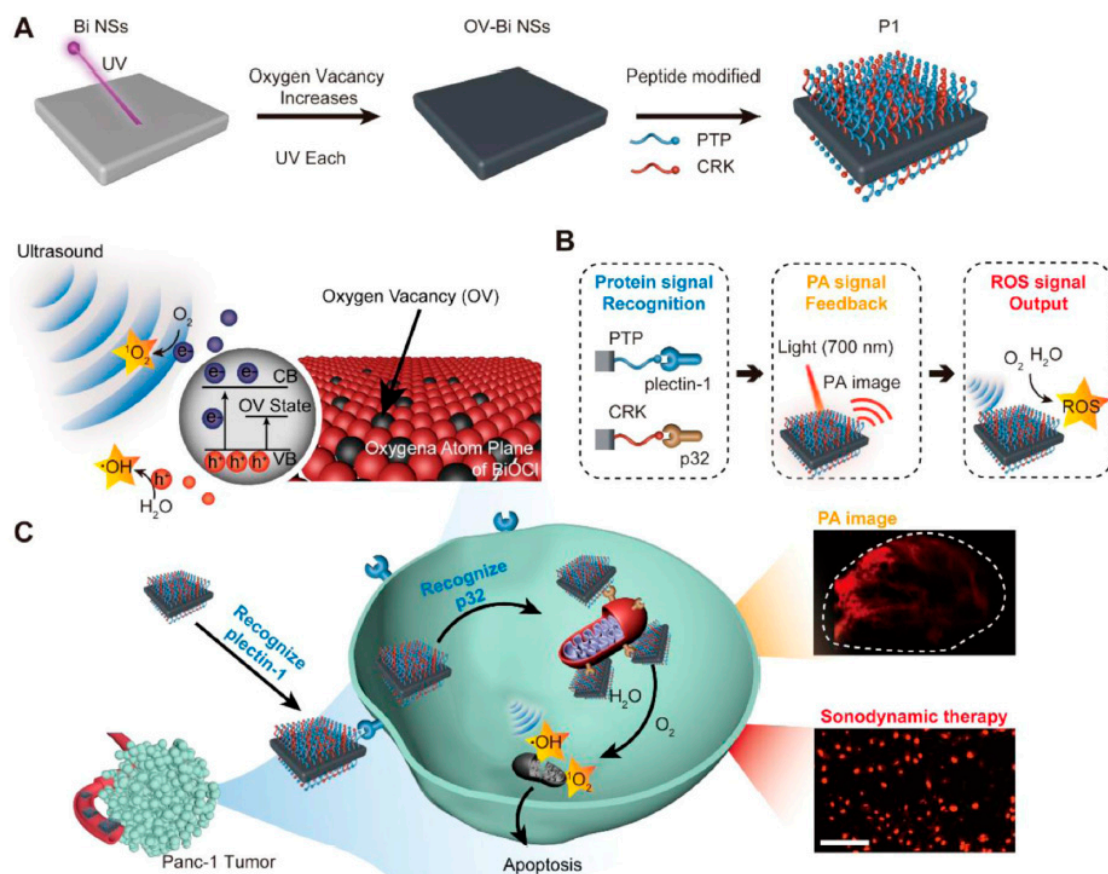


Figure 11. BiOCl nanosheets used for PA imaging-guided SDT. (A) Fabrication of oxygen-vacancy-rich BiOCl NSs modified with PTP and CRK; (B) scheme of cancer cell and mitochondrial targeting, PA imaging, and ROS generation capabilities; (C) scheme of PA imaging-guided SDT of oxygen-vacancy-rich BiOCl NSs. Reproduced with permission from Ref. [66], 2021, Elsevier.

X-ray is another method for stimulating semiconductors to produce ROS, due to its higher energy. This is especially true for bismuth-based semiconductors, as they have stronger X-ray absorption abilities due to high atomic numbers (83) and the X-ray attenuation coefficient ($4.3 \text{ cm}^2 \text{ g}^{-1}$ at 100 keV) of Bi elements. In fact, there have been some bismuth-based NMs used for radiation therapy, such as Bi_2S_3 [116], Bi_2Se_3 [117], Bi_2O_3 [118], BiOI [70], pure Bi [119], and BiOCl NMs [120]. However, the radiation therapy efficacy has been limited by the tumor microenvironment of solid tumors, such as

hypoxia and antioxidative GSH. In order to improve therapeutic efficacy, Li's group designed hydrogen peroxide (H_2O_2)-loaded Cu-doped BiOCl nanocomposites (BCHN) to improve the synergistic effect of radiation and chemodynamic therapy through modulating the tumor microenvironment [120]. BCHN were fabricated through a stepwise method. First, $Na_{0.2}Bi_{0.8}O_{0.35}F_{1.91}$ (NBOF) was obtained through co-precipitation of sodium nitrate, bismuth nitrate, and ammonium fluoride. Then, Cu^{2+} was absorbed on the surface of NBOF. After adding sodium hydroxide and H_2O_2 , BCHN monodispersed mesoporous nanospheres were obtained, as proved by the XRD pattern (Figure 12A) and SEM image (Figure 12B). The existence of Cu^{2+} and H_2O_2 in BCHN has been confirmed by Cu 2p high-resolution XPS spectrum (Figure 12C) and the redox reaction of potassium permanganate and H_2O_2 (Figure 12D). Intracellular GSH and O_2 levels showed that BCHN could effectively deplete GSH (Figure 12E) and produce O_2 (Figure 12F) through Fenton-like reactions among Cu^{2+} , GSH, and H_2O_2 . Therefore, without radiation, BCHN alone could kill some cancer cells due to the chemodynamic property, as well as change the antioxidant and hypoxic microenvironment, while with radiation, BCHN could effectively produce ROS to kill the other cancer cells (Figure 12G). In vivo experiments further proved that BCHN could be used as a synergistic radiation therapy/chemotherapy agent with good biocompatibility.

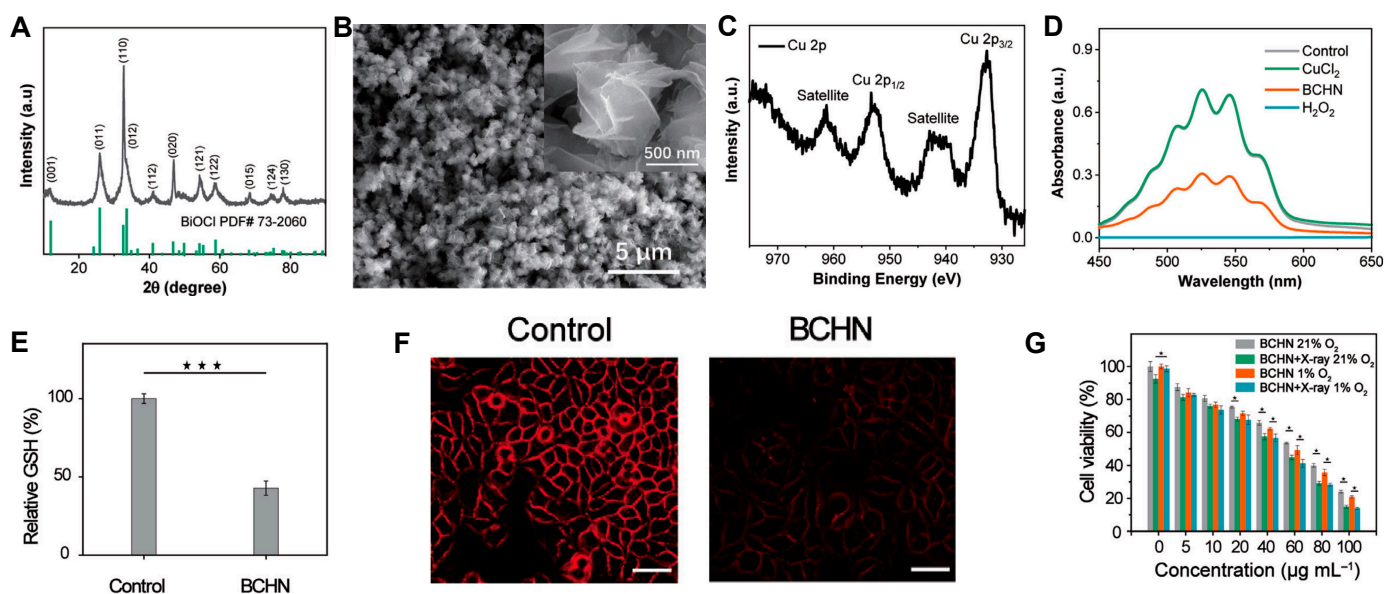


Figure 12. Hydrogen peroxide (H_2O_2)-loaded Cu-doped BiOCl nanocomposite (BCHN) to improve synergistic effect of radiation and chemodynamic therapy through modulating tumor microenvironment. (A–C) XRD pattern (A), SEM image (B), and XPS spectra (C) of BCHN. (D) UV–vis absorption spectra of $KMnO_4$ solution ($50 \mu g mL^{-1}$) after adding $CuCl_2$, BCHN, and H_2O_2 , respectively ($0.1 M H_2SO_4$, reaction time = 10 min). (E–F) Relative GSH content (E) and oxygen levels (F) in 4T1.2 cells without or with BCHN incubation. (G) Relative viability of 4T1.2 cells incubated with BCHN and further radiated with or without X-rays under normoxic and hypoxic conditions. Reproduced with permission from Ref. [120], 2021, Elsevier.

4. Conclusions and Perspectives

In this review, we summarized the recent progress of BiOCl NMs, from degradation to biomedical applications. As typical 2D NMs, BiOCl can effectively generate ROS, which can be used for simulating sunlight-triggered pollution degradation, bacterial inactivation, biosensing, and cancer therapy. Regulating the morphologies and forming heterostructures are the two main and effective methods for improving ROS generation efficacy, because both methods could not only narrow the bandgap of BiOCl for more light absorption, but also facilitate photoinduced electron and hole separation. However, the biomedical application of BiOCl NMs still needs to be development. There exist some challenges that

need to be investigated and addressed to promote the practical application of theranostic BiOCl-based NMs. (1) Being used as nanomedicine, the biosafety and biocompatibility needs to be systematically investigated. (2) As typical 2D NMs with various morphologies, BiOCl-based nanocarriers with responsive releasing performance for treating different diseases need to be developed. (3) BiOCl-based NMs could kill effective bacteria due to the excellent ROS production ability; however, few studies have applied them to in vivo diseases. Therefore, BiOCl-based antibacterial agents could be further used for various bacterial invasion diseases, such as wound healing, cholera, pneumonia, and influenza. (4) Bi-containing NMs have good performance for CT imaging; however, the CT imaging application of BiOCl-based NMs is rare. As a result, more BiOCl-based NMs need to be developed for bioimaging. (5) Although BiOCl-based NMs have been used for cancer therapy, the NIR-activating ability needs to be realized. Moreover, more strategies need to be developed for improving cancer therapy efficacy. (6) As a type of semiconductor, BiOCl could also be activated by ultrasound and X-ray. As a result, BiOCl-based sonodynamic therapy and radiation therapy should be developed.

Author Contributions: Conceptualization, R.C.; writing—original draft preparation, L.W., Y.L., G.C., M.Z., X.Y., R.C. and Y.C.; writing—review and editing, R.C. and Y.C.; supervision, R.C. and Y.C.; funding acquisition, L.W., X.Y., R.C. and Y.C. All authors have read and agreed to the published version of the manuscript.

Funding: This research was funded by Natural Science Foundation of China (No. 32171396), Science and Technology Development Project Foundation of Jilin Province (No. YDZJ202101ZYTS108, 20200201023JC), Science and Technology Innovation Team Foundation of Jilin Province (No. 20210509-044RQ), Scientific and Technological Project of Jilin Provincial Department of Education (No. JJKH2021-0612KJ), China Postdoctoral Science Foundation (No. 2021M691191), and Changchun University (No. zkp202119).

Institutional Review Board Statement: Not applicable.

Informed Consent Statement: Not applicable.

Data Availability Statement: The study does not report new data.

Conflicts of Interest: The authors declare no conflict of interest.

References

1. Tong, H.; Ouyang, S.; Bi, Y.; Umezawa, N.; Oshikiri, M.; Ye, J. Nano-photocatalytic materials: Possibilities and challenges. *Adv. Mater.* **2012**, *24*, 229–251. [[CrossRef](#)] [[PubMed](#)]
2. Chen, X.; Liu, L.; Yu, P.Y.; Mao, S.S. Increasing solar absorption for photocatalysis with black hydrogenated titanium dioxide nanocrystals. *Science* **2011**, *331*, 746–750. [[CrossRef](#)] [[PubMed](#)]
3. Chong, M.N.; Jin, B.; Chow, C.W.; Saint, C. Recent developments in photocatalytic water treatment technology: A review. *Water Res.* **2010**, *44*, 2997–3027. [[CrossRef](#)] [[PubMed](#)]
4. Linic, S.; Christopher, P.; Ingram, D.B. Plasmonic-metal nanostructures for efficient conversion of solar to chemical energy. *Nat. Mater.* **2011**, *10*, 911–921. [[CrossRef](#)]
5. Ni, M.; Leung, M.K.H.; Leung, D.Y.C.; Sumathy, K. A review and recent developments in photocatalytic water-splitting using TiO₂ for hydrogen production. *Renew. Sustain. Energy Rev.* **2007**, *11*, 401–425. [[CrossRef](#)]
6. Chen, X.; Shen, S.; Guo, L.; Mao, S.S. Semiconductor-based photocatalytic hydrogen generation. *Chem. Rev.* **2010**, *110*, 6503–6570. [[CrossRef](#)]
7. Wu, M.; Huang, H.; Leung, D.Y.C. A review of volatile organic compounds (VOCs) degradation by vacuum ultraviolet (VUV) catalytic oxidation. *J. Environ. Manage.* **2022**, *307*, 114559. [[CrossRef](#)]
8. Xu, Z.; Ao, Z.; Yang, M.; Wang, S. Recent progress in single-atom alloys: Synthesis, properties, and applications in environmental catalysis. *J. Hazard. Mater.* **2022**, *424*, 127427. [[CrossRef](#)]
9. Saravanan, A.; Kumar, P.S.; Jeevanantham, S.; Anubha, M.; Jayashree, S. Degradation of toxic agrochemicals and pharmaceutical pollutants: Effective and alternative approaches toward photocatalysis. *Environ. Pollut.* **2022**, *298*, 118844. [[CrossRef](#)]
10. Saya, L.; Malik, V.; Gautam, D.; Gambhir, G.; Singh, W.R.; Hooda, S. A comprehensive review on recent advances toward sequestration of levofloxacin antibiotic from wastewater. *Sci. Total Environ.* **2022**, *813*, 152529. [[CrossRef](#)]
11. Khin, M.M.; Nair, A.S.; Babu, V.J.; Murugan, R.; Ramakrishna, S. A review on nanomaterials for environmental remediation. *Energy Environ. Sci.* **2012**, *5*, 8075–8109. [[CrossRef](#)]

12. Baran, W.; Adamek, E.; Ziemianska, J.; Sobczak, A. Effects of the presence of sulfonamides in the environment and their influence on human health. *J. Hazard. Mater.* **2011**, *196*, 1–15. [[CrossRef](#)] [[PubMed](#)]
13. Barakat, M.A. New trends in removing heavy metals from industrial wastewater. *Arab. J. Chem.* **2011**, *4*, 361–377. [[CrossRef](#)]
14. Xu, P.; Zeng, G.M.; Huang, D.L.; Feng, C.L.; Hu, S.; Zhao, M.H.; Lai, C.; Wei, Z.; Huang, C.; Xie, G.X.; et al. Use of iron oxide nanomaterials in wastewater treatment: A review. *Sci. Total Environ.* **2012**, *424*, 1–10. [[CrossRef](#)]
15. Uyguner Demirel, C.S.; Birben, N.C.; Bekbolet, M. A comprehensive review on the use of second generation TiO₂ photocatalysts: Microorganism inactivation. *Chemosphere* **2018**, *211*, 420–448. [[CrossRef](#)] [[PubMed](#)]
16. Josset, S.; Keller, N.; Lett, M.C.; Ledoux, M.J.; Keller, V. Numeration methods for targeting photoactive materials in the UV-A photocatalytic removal of microorganisms. *Chem. Soc. Rev.* **2008**, *37*, 744–755. [[CrossRef](#)]
17. Chen, R.; Xie, Y.; Meng, S.; Yan, Y.; Yang, Q.; Wang, L.; Wang, X. Protoporphyrin IX functionalized α -Fe₂O₃ for enhanced photocatalytic and antimicrobial activity under sunlight. *Funct. Mater. Lett.* **2019**, *12*, 1950079. [[CrossRef](#)]
18. Zinatloo-Ajabshir, S.; Baladi, M.; Salavati-Niasari, M. Sono-synthesis of MnWO₄ ceramic nanomaterials as highly efficient photocatalysts for the decomposition of toxic pollutants. *Ceram. Int.* **2021**, *47*, 30178–30187. [[CrossRef](#)]
19. Zinatloo-Ajabshir, S.; Baladi, M.; Salavati-Niasari, M. Enhanced visible-light-driven photocatalytic performance for degradation of organic contaminants using PbWO₄ nanostructure fabricated by a new, simple and green sonochemical approach. *Ultrason. Sonochem.* **2021**, *72*, 105420. [[CrossRef](#)]
20. Chen, R.; Xie, Y.B.; Chen, G.L.; Yang, X.D.; Lu, X.; Wang, L.L. Phase, optical property, and photocatalytic performance behaviors of non-stoichiometric bismuth oxyiodide. *Inorg. Nano-Metal. Chem.* **2021**, *51*, 1226–1231. [[CrossRef](#)]
21. Wang, L.; Meng, S.; Chen, G.; Yang, X.; Yan, Y.; Chen, R. Relationship between secondary phase and photocatalytic activity in titanium-doped bismuth ferrite nanocrystals. *Micro Nano Lett.* **2020**, *15*, 713–716. [[CrossRef](#)]
22. Craciun, A.M.; Focsan, M.; Magyari, K.; Vulpoi, A.; Pap, Z. Surface Plasmon Resonance or Biocompatibility-Key Properties for Determining the Applicability of Noble Metal Nanoparticles. *Materials* **2017**, *10*, 836. [[CrossRef](#)] [[PubMed](#)]
23. Pal, K.; Asthana, N.; Aljabali, A.A.; Bhardwaj, S.K.; Kralj, S.; Penkova, A.; Thomas, S.; Zaheer, T.; de Souza, F.G. A critical review on multifunctional smart materials ‘nanographene’ emerging avenue: Nano-imaging and biosensor applications. *Crit. Rev. Solid State Mater. Sci.* **2021**, 1–17. [[CrossRef](#)]
24. Cheng, Y.; Zhang, H.Y. Novel Bismuth-Based Nanomaterials Used for Cancer Diagnosis and Therapy. *Chem.—A Eur. J.* **2018**, *24*, 17405–17418. [[CrossRef](#)] [[PubMed](#)]
25. Cheng, Y.; Chang, Y.; Feng, Y.; Jian, H.; Wu, X.; Zheng, R.; Xu, K.; Zhang, H. Bismuth Sulfide Nanorods with Retractable Zinc Protoporphyrin Molecules for Suppressing Innate Antioxidant Defense System and Strengthening Phototherapeutic Effects. *Adv. Mater.* **2019**, *31*, 1806808. [[CrossRef](#)] [[PubMed](#)]
26. Cheng, Y.; Kong, X.; Chang, Y.; Feng, Y.; Zheng, R.; Wu, X.; Xu, K.; Gao, X.; Zhang, H. Spatiotemporally Synchronous Oxygen Self-Supply and Reactive Oxygen Species Production on Z-Scheme Heterostructures for Hypoxic Tumor Therapy. *Adv. Mater.* **2020**, *32*, e1908109. [[CrossRef](#)] [[PubMed](#)]
27. Li, Y.; Jiang, H.Y.; Wang, X.; Hong, X.D.; Liang, B. Recent advances in bismuth oxyhalide photocatalysts for degradation of organic pollutants in wastewater. *RSC Adv.* **2021**, *11*, 26855–26875. [[CrossRef](#)]
28. Wang, Z.W.; Chen, M.; Huang, D.L.; Zeng, G.M.; Xu, P.; Zhou, C.Y.; Lai, C.; Wang, H.; Cheng, M.; Wang, W.J. Multiply structural optimized strategies for bismuth oxyhalide photocatalysis and their environmental application. *Chem. Eng. J.* **2019**, *374*, 1025–1045. [[CrossRef](#)]
29. Younis, M.R.; He, G.; Qu, J.; Lin, J.; Huang, P.; Xia, X.H. Inorganic Nanomaterials with Intrinsic Singlet Oxygen Generation for Photodynamic Therapy. *Adv. Sci.* **2021**, *8*, e2102587. [[CrossRef](#)]
30. Zemann, J. Crystal structures, 2nd edition. Vol. 1 by R. W. G. Wyckoff. *Acta Crystallogr.* **1965**, *18*, 139. [[CrossRef](#)]
31. Li, H.; Li, J.; Ai, Z.; Jia, F.; Zhang, L. Oxygen Vacancy-Mediated Photocatalysis of BiOCl: Reactivity, Selectivity, and Perspectives. *Angew Chem. Int. Ed. Engl.* **2018**, *57*, 122–138. [[CrossRef](#)] [[PubMed](#)]
32. Ren, Q.; Liu, J.M.; Yang, Q.; Shen, W. A Review: Photocatalysts Based on BiOCl and g-C₃N₄ for Water Purification. *Catalysts* **2021**, *11*, 1084. [[CrossRef](#)]
33. Yang, X.L.; Sun, S.D.; Cui, J.; Yang, M.; Luo, Y.G.; Liang, S.H. Synthesis, Functional Modifications, and Diversified Applications of Hybrid BiOCl-Based Heterogeneous Photocatalysts: A Review. *Cryst. Growth Des.* **2021**, *21*, 6576–6618. [[CrossRef](#)]
34. Xiao, X.; Liu, C.; Hu, R.; Zuo, X.; Nan, J.; Li, L.; Wang, L. Oxygen-rich bismuth oxyhalides: Generalized one-pot synthesis, band structures and visible-light photocatalytic properties. *J. Mater. Chem.* **2012**, *22*, 22840. [[CrossRef](#)]
35. Li, M.; Zhang, J.; Gao, H.; Li, F.; Lindquist, S.E.; Wu, N.; Wang, R. Microsized BiOCl Square Nanosheets as Ultraviolet Photodetectors and Photocatalysts. *ACS Appl. Mater. Interfaces* **2016**, *8*, 6662–6668. [[CrossRef](#)]
36. Lei, Y.Q.; Wang, G.H.; Song, S.Y.; Fan, W.Q.; Zhang, H.J. Synthesis, characterization and assembly of BiOCl nanostructure and their photocatalytic properties. *Crystengcomm* **2009**, *11*, 1857–1862. [[CrossRef](#)]
37. Cai, Y.J.; Li, D.Y.; Sun, J.Y.; Chen, M.D.; Li, Y.R.; Zou, Z.W.; Zhang, H.; Xu, H.M.; Xia, D.S. Synthesis of BiOCl nanosheets with oxygen vacancies for the improved photocatalytic properties. *Appl. Surf. Sci.* **2018**, *439*, 697–704. [[CrossRef](#)]
38. Hou, J.H.; Dai, D.; Wei, R.; Wu, X.G.; Wang, X.Z.; Tahir, M.; Zou, J.J. Narrowing the Band Gap of BiOCl for the Hydroxyl Radical Generation of Photocatalysis under Visible Light. *ACS Sustain. Chem. Eng.* **2019**, *7*, 16569–16576. [[CrossRef](#)]
39. Cheng, G.; Xiong, J.Y.; Stadler, F.J. Facile template-free and fast refluxing synthesis of 3D desertrose-like BiOCl nanoarchitectures with superior photocatalytic activity. *New J. Chem.* **2013**, *37*, 3207–3213. [[CrossRef](#)]

40. Hu, J.L.; Fan, W.J.; Ye, W.Q.; Huang, C.J.; Qiu, X.Q. Insights into the photosensitivity activity of BiOCl under visible light irradiation. *Appl. Catal. B Environ.* **2014**, *158*, 182–189. [[CrossRef](#)]
41. Zhu, L.P.; Liao, G.H.; Bing, N.C.; Wang, L.L.; Yang, Y.; Xie, H.Y. Self-assembled 3D BiOCl architectures: Tunable synthesis and characterization. *Crystengcomm* **2010**, *12*, 3791–3796. [[CrossRef](#)]
42. Xiong, J.; Cheng, G.; Li, G.; Qin, F.; Chen, R. Well-crystallized square-like 2D BiOCl nanoplates: Mannitol-assisted hydrothermal synthesis and improved visible-light-driven photocatalytic performance. *RSC Adv.* **2011**, *1*, 1542–1553. [[CrossRef](#)]
43. Zhang, K.; Liang, J.; Wang, S.; Liu, J.; Ren, K.X.; Zheng, X.; Luo, H.; Peng, Y.J.; Zou, X.; Bo, X.; et al. BiOCl Sub-Microcrystals Induced by Citric Acid and Their High Photocatalytic Activities. *Cryst. Growth Des.* **2012**, *12*, 793–803. [[CrossRef](#)]
44. Wu, S.J.; Wang, C.; Cui, Y.F.; Hao, W.C.; Wang, T.M.; Brault, P. BiOCl nano/microstructures on substrates: Synthesis and photocatalytic properties. *Mater. Lett.* **2011**, *65*, 1344–1347. [[CrossRef](#)]
45. Wu, S.J.; Wang, C.; Cui, Y.F.; Wang, T.M.; Huang, B.B.; Zhang, X.Y.; Qin, X.Y.; Brault, P. Synthesis and photocatalytic properties of BiOCl nanowire arrays. *Mater. Lett.* **2010**, *64*, 115–118. [[CrossRef](#)]
46. Tian, J.; Chen, Z.Y.; Jing, J.P.; Feng, C.; Sun, M.M.; Li, W.B. Enhanced photocatalytic activity of BiOCl with regulated morphology and band structure through controlling the adding amount of HCl. *Mater. Lett.* **2020**, *272*, 127860. [[CrossRef](#)]
47. Cui, P.Z.; Wang, J.L.; Wang, Z.M.; Chen, J.; Xing, X.R.; Wang, L.Z.; Yu, R.B. Bismuth oxychloride hollow microspheres with high visible light photocatalytic activity. *Nano Res.* **2016**, *9*, 593–601. [[CrossRef](#)]
48. Xiong, J.Y.; Cheng, G.; Qin, F.; Wang, R.M.; Sun, H.Z.; Chen, R. Tunable BiOCl hierarchical nanostructures for high-efficient photocatalysis under visible light irradiation. *Chem. Eng. J.* **2013**, *220*, 228–236. [[CrossRef](#)]
49. Ma, X.; Cheng, Y.; Jian, H.; Feng, Y.; Chang, Y.; Zheng, R.; Wu, X.; Wang, L.; Li, X.; Zhang, H. Hollow, Rough, and Nitric Oxide-Releasing Cerium Oxide Nanoparticles for Promoting Multiple Stages of Wound Healing. *Adv. Healthc. Mater.* **2019**, *8*, e1900256. [[CrossRef](#)]
50. Liu, N.; Chang, Y.; Feng, Y.; Cheng, Y.; Sun, X.; Jian, H.; Feng, Y.; Li, X.; Zhang, H. {101}-[001] Surface Heterojunction-Enhanced Antibacterial Activity of Titanium Dioxide Nanocrystals Under Sunlight Irradiation. *ACS Appl. Mater. Interfaces* **2017**, *9*, 5907–5915. [[CrossRef](#)]
51. Zhao, H.; Liu, X.; Dong, Y.; Xia, Y.; Wang, H.; Zhu, X. Fabrication of a Z-Scheme {001}/{110} Facet Heterojunction in BiOCl to Promote Spatial Charge Separation. *ACS Appl. Mater. Interfaces* **2020**, *12*, 31532–31541. [[CrossRef](#)] [[PubMed](#)]
52. Heidari, S.; Haghighi, M.; Shabani, M. Sunlight-activated BiOCl/BiOBr-Bi₂₄O₃₁Br₁₀ photocatalyst for the removal of pharmaceutical compounds. *J. Clean. Prod.* **2020**, *259*, 120679. [[CrossRef](#)]
53. Jia, X.; Cao, J.; Lin, H.; Zhang, M.; Guo, X.; Chen, S. Transforming type-I to type-II heterostructure photocatalyst via energy band engineering: A case study of I-BiOCl/I-BiOBr. *Appl. Catal. B Environ.* **2017**, *204*, 505–514. [[CrossRef](#)]
54. Chang, X.; Yu, G.; Huang, J.; Li, Z.; Zhu, S.; Yu, P.; Cheng, C.; Deng, S.; Ji, G. Enhancement of photocatalytic activity over NaBiO₃/BiOCl composite prepared by an in situ formation strategy. *Catal. Today* **2010**, *153*, 193–199. [[CrossRef](#)]
55. Duo, F.; Wang, Y.; Mao, X.; Zhang, X.; Wang, Y.; Fan, C. A BiPO₄/BiOCl heterojunction photocatalyst with enhanced electron-hole separation and excellent photocatalytic performance. *Appl. Surf. Sci.* **2015**, *340*, 35–42. [[CrossRef](#)]
56. He, Z.; Shi, Y.; Gao, C.; Wen, L.; Chen, J.; Song, S. BiOCl/BiVO₄ p-n Heterojunction with Enhanced Photocatalytic Activity under Visible-Light Irradiation. *J. Phys. Chem. C* **2014**, *118*, 389–398. [[CrossRef](#)]
57. Liu, F.-Y.; Jiang, Y.-R.; Chen, C.-C.; Lee, W.W. Novel synthesis of PbBiO₂Cl/BiOCl nanocomposite with enhanced visible-driven-light photocatalytic activity. *Catal. Today* **2018**, *300*, 112–123. [[CrossRef](#)]
58. Sun, Y.; Qi, X.; Li, R.; Xie, Y.; Tang, Q.; Ren, B. Hydrothermal synthesis of 2D/2D BiOCl/g-C₃N₄ Z-scheme: For TC degradation and antimicrobial activity evaluation. *Opt. Mater.* **2020**, *108*, 110170. [[CrossRef](#)]
59. Gao, X.; Tang, G.; Peng, W.; Guo, Q.; Luo, Y. Surprise in the phosphate modification of BiOCl with oxygen vacancy: In situ construction of hierarchical Z-scheme BiOCl-OV-BiPO₄ photocatalyst for the degradation of carbamazepine. *Chem. Eng. J.* **2019**, *360*, 1320–1329. [[CrossRef](#)]
60. Li, Q.; Guan, Z.; Wu, D.; Zhao, X.; Bao, S.; Tian, B.; Zhang, J. Z-Scheme BiOCl-Au-CdS Heterostructure with Enhanced Sunlight-Driven Photocatalytic Activity in Degrading Water Dyes and Antibiotics. *ACS Sustain. Chem. Eng.* **2017**, *5*, 6958–6968. [[CrossRef](#)]
61. Gorbach, S.L. Bismuth therapy in gastrointestinal diseases. *Gastroenterology* **1990**, *99*, 863–875. [[CrossRef](#)]
62. Bierer, D.W. Bismuth subsalicylate: History, chemistry, and safety. *Rev. Infect. Dis.* **1990**, *12* (Suppl. 1), S3–S8. [[CrossRef](#)] [[PubMed](#)]
63. Deng, J.; Mo, Y.; Liu, J.; Guo, R.; Zhang, Y.; Xue, W.; Zhang, Y. In Vitro Study of SnS₂, BiOCl and SnS₂-Incorporated BiOCl Inorganic Nanoparticles Used as Doxorubicin Carrier. *J. Nanosci. Nanotechnol.* **2016**, *16*, 5740–5745. [[CrossRef](#)] [[PubMed](#)]
64. Chen, X.; Wang, R.; Liu, D.; Tian, Y.; Ye, L. Prussian Blue Analogue Islands on BiOCl-Se Nanosheets for MR/CT Imaging-Guided Photothermal/Photodynamic Cancer Therapy. *ACS Appl. Biol. Mater.* **2019**, *2*, 1213–1224. [[CrossRef](#)] [[PubMed](#)]
65. Dai, C.; Hu, R.; Wang, C.; Liu, Z.; Zhang, S.; Yu, L.; Chen, Y.; Zhang, B. Defect engineering of 2D BiOCl nanosheets for photonic tumor ablation. *Nanoscale Horiz.* **2020**, *5*, 857–868. [[CrossRef](#)]
66. Zhang, X.H.; Guo, R.C.; Chen, Y.F.; Xu, X.; Yang, Z.X.; Cheng, D.B.; Chen, H.; Qiao, Z.Y.; Wang, H. A BiOCl nanodevice for pancreatic tumor imaging and mitochondria-targeted therapy. *Nano Today* **2021**, *40*, 101285. [[CrossRef](#)]
67. Jang, J.; Kim, K.; Yoon, J.; Park, C.B. Piezoelectric materials for ultrasound-driven dissociation of Alzheimer's beta-amyloid aggregate structure. *Biomaterials* **2020**, *255*, 120165. [[CrossRef](#)]

68. Ma, S.; Wang, L.; Liu, Z.; Luo, X.; Zhou, Z.; Xie, J.; Li, Y.; Cong, S.; Zhou, M.; Xu, Y.; et al. "One stone, two birds": Engineering 2-D ultrathin heterostructure nanosheet BiNS@NaLnF₄ for dual-modal computed tomography/magnetic resonance imaging guided, photonic synergetic theranostics. *Nanoscale* **2021**, *13*, 185–194. [CrossRef]
69. Wang, H.; Yang, W.; Bian, K.; Zeng, W.; Jin, X.; Ouyang, R.; Xu, Y.; Dai, C.; Zhou, S.; Zhang, B. Oxygen-Deficient BiOCl Combined with L-Buthionine-Sulfoximine Synergistically Suppresses Tumor Growth through Enhanced Singlet Oxygen Generation under Ultrasound Irradiation. *Small* **2021**, *18*, e2104550. [CrossRef]
70. Guo, Z.; Zhu, S.; Yong, Y.; Zhang, X.; Dong, X.; Du, J.; Xie, J.; Wang, Q.; Gu, Z.; Zhao, Y. Synthesis of BSA-Coated BiOI@Bi₂S₃ Semiconductor Heterojunction Nanoparticles and Their Applications for Radio/Photodynamic/Photothermal Synergistic Therapy of Tumor. *Adv. Mater.* **2017**, *29*, 1704136. [CrossRef]
71. Xu, L.; He, F.; Wang, C.; Gai, S.; Gulzar, A.; Yang, D.; Zhong, C.; Yang, P. Lanthanide-doped bismuth oxobromide nanosheets for self-activated photodynamic therapy. *J. Mater. Chem. B* **2017**, *5*, 7939–7948. [CrossRef] [PubMed]
72. Zhao, W.W.; Xu, J.J.; Chen, H.Y. Photoelectrochemical aptasensing. *TrAC Trends Anal. Chem.* **2016**, *82*, 307–315. [CrossRef]
73. Xu, L.; Yan, P.C.; Li, H.N.; Ling, S.Y.; Xia, J.X.; Qiu, J.X.; Xu, Q.; Li, H.M.; Yuan, S.Q. Metallic Bi self-doping BiOCl composites: Synthesis and enhanced photoelectrochemical performance. *Mater. Lett.* **2017**, *196*, 225–229. [CrossRef]
74. Xu, L.; Li, H.; Yan, P.; Xia, J.; Qiu, J.; Xu, Q.; Zhang, S.; Li, H.; Yuan, S. Graphitic carbon nitride/BiOCl composites for sensitive photoelectrochemical detection of ciprofloxacin. *J. Colloid Interface Sci.* **2016**, *483*, 241–248. [CrossRef]
75. Yang, M.; Chen, Y.; Yan, P.; Dong, J.; Duan, W.; Xu, L.; Li, H. A photoelectrochemical aptasensor of ciprofloxacin based on Bi₂O₃/BiOCl heterojunction. *Mikrochim. Acta* **2021**, *188*, 289. [CrossRef]
76. Xu, L.; He, X.; Dong, J.; Yan, P.; Chen, F.; Zhang, J.; Li, H. A photoelectrochemical aptasensor for sensitively monitoring chloramphenicol using plasmon-driven AgNP/BiOCl composites. *Analyst* **2020**, *145*, 7695–7700. [CrossRef]
77. Zeng, R.; Luo, Z.; Su, L.; Zhang, L.; Tang, D.; Niessner, R.; Knopp, D. Palindromic Molecular Beacon Based Z-Scheme BiOCl-Au-CdS Photoelectrochemical Biodetection. *Anal. Chem.* **2019**, *91*, 2447–2454. [CrossRef]
78. Yan, P.C.; Mo, Z.; Dong, J.T.; Chen, F.; Qian, J.C.; Xia, J.X.; Xu, L.; Zhang, J.M.; Li, H.N. Construction of Mn valence-engineered MnO₂/BiOCl heterojunction coupled with carriers-trapping effect for enhanced photoelectrochemical lincomycin aptasensor. *Sens. Actuators B-Chem.* **2020**, *320*, 128415. [CrossRef]
79. Yan, P.; Xu, L.; Xia, J.; Huang, Y.; Qiu, J.; Xu, Q.; Zhang, Q.; Li, H. Photoelectrochemical sensing of 4-chlorophenol based on Au/BiOCl nanocomposites. *Talanta* **2016**, *156–157*, 257–264. [CrossRef]
80. Yan, P.C.; Jiang, D.S.; Li, H.N.; Biao, J.; Xu, L.; Qian, J.C.; Chen, C.; Xia, J.X. BiPO₄ nanocrystal/BiOCl nanosheet heterojunction as the basis for a photoelectrochemical 4-chlorophenol sensor. *Sens. Actuators B-Chem.* **2019**, *279*, 466–475. [CrossRef]
81. Wang, H.; Zhang, B.; Zhao, F.; Zeng, B. One-Pot Synthesis of N-Graphene Quantum Dot-Functionalized I-BiOCl Z-Scheme Cathodic Materials for "Signal-Off" Photoelectrochemical Sensing of Chlorpyrifos. *ACS Appl. Mater. Interfaces* **2018**, *10*, 35281–35288. [CrossRef] [PubMed]
82. Luo, Y.N.; Mi, Y.; Tan, X.C.; Chen, Q.Y.; Feng, D.F.; Ai, C.H. Ultrathin BiOCl nanosheet modified TiO₂ for the photoelectrochemical sensing of chlorpyrifos. *Anal. Methods* **2019**, *11*, 375–380. [CrossRef]
83. Yan, X.R.; Li, J.; Kong, L.F.; Li, M.Y.; Li, H.L.; Qian, C.; Wang, M.; Zhang, X.F.; Lu, Y.; Han, J.Y.; et al. AuNPs/g-C₃N₄/BiOCl_{0.5}Br_{0.5} Heterojunction Sensitizing Sensor for Photoelectrochemical Sensing of 2-Chloroethyl Phosphoric Acid. *Chin. J. Anal. Chem.* **2021**, *49*, 797–805. [CrossRef]
84. Gopalan, A.I.; Muthuchamy, N.; Lee, K.P. A novel bismuth oxychloride-graphene hybrid nanosheets based non-enzymatic photoelectrochemical glucose sensing platform for high performances. *Biosens. Bioelectron.* **2017**, *89*, 352–360. [CrossRef] [PubMed]
85. Liu, H.P.; Xu, G.Q.; Wang, J.W.; Lv, J.; Zheng, Z.X.; Wu, Y.C. Photoelectrochemical properties of TiO₂ Nanotube Arrays Modified with BiOCl nanosheets. *Electrochim. Acta* **2014**, *130*, 213–221. [CrossRef]
86. Ijaz, H.; Zia, R.; Taj, A.; Jameel, F.; Butt, F.K.; Asim, T.; Jameel, N.; Abbas, W.; Iqbal, M.; Bajwa, S.Z.; et al. Synthesis of BiOCl nanoplatelets as the dual interfaces for the detection of glutathione linked disease biomarkers and biocompatibility assessment in vitro against HCT cell lines model. *Appl. Nanosci.* **2020**, *10*, 3569–3576. [CrossRef]
87. Li, H.A.; Zhu, M.Y.; Chen, W.; Wang, K. Ternary heterojunctions composed of BiOCl, BiVO₄ and nitrogen-doped carbon quantum dots for use in photoelectrochemical sensing: Effective charge separation and application to ultrasensitive sensing of dopamine. *Mikrochim. Acta* **2017**, *184*, 4827–4833. [CrossRef]
88. Yu, L.D.; Wang, Y.N.; Zhang, X.Y.; Li, N.A.B.; Luo, H.Q. A novel signal-on photoelectrochemical platform for highly sensitive detection of alkaline phosphatase based on dual Z-scheme CdS/Bi₂S₃/BiOCl composites. *Sens. Actuators B-Chem.* **2021**, *340*, 129988. [CrossRef]
89. Zhang, B.; Jia, Y.; Wang, J.; Hu, X.; Zhao, Z.; Cheng, Y. Cysteine-assisted photoelectrochemical immunoassay for the carcinoembryonic antigen by using an ITO electrode modified with C₃N₄-BiOCl semiconductor and CuO nanoparticles as antibody labels. *Mikrochim. Acta* **2019**, *186*, 633. [CrossRef]
90. Wang, H.; Zhang, B.; Xi, J.; Zhao, F.; Zeng, B. Z-scheme I-BiOCl/CdS with abundant oxygen vacancies as highly effective cathodic material for photocathodic immunoassay. *Biosens. Bioelectron.* **2019**, *141*, 111443. [CrossRef]
91. Mao, L.B.; Liu, H.; Yao, L.L.; Wen, W.; Chen, M.M.; Zhang, X.H.; Wang, S.F. Construction of a dual-functional CuO/BiOCl heterojunction for high-efficiently photoelectrochemical biosensing and photoelectrocatalytic degradation of aflatoxin B1. *Chem. Eng. J.* **2022**, *429*, 132297. [CrossRef]

92. Song, Y.Y.; Jiang, H.J.; Shi, X.Y.; Chen, J.; Wu, Y.; Wei, W. Detection of Lead Using a Sensitive Anodic Stripping Voltammetric Method Based on Composite Mesoporous Silica/Bismuth Oxychloride Modified Electrode. *Chemistryselect* **2018**, *3*, 2423–2429. [[CrossRef](#)]
93. Jahani, P.M.; Javar, H.A.; Mahmoudi-Moghaddam, H. Development of a novel electrochemical sensor using the FeNi₃/CuS/BiOCl nanocomposite for determination of naproxen. *J. Mater. Sci.-Mater. Electron.* **2020**, *31*, 14022–14034. [[CrossRef](#)]
94. Gao, J.; Liu, M.; Song, H.; Zhang, S.; Qian, Y.; Li, A. Highly-sensitive electrocatalytic determination for toxic phenols based on coupled cMWCNT/cyclodextrin edge-functionalized graphene composite. *J. Hazard. Mater.* **2016**, *318*, 99–108. [[CrossRef](#)]
95. Pitz, A.M.; Park, G.W.; Lee, D.; Boissy, Y.L.; Vinje, J. Antimicrobial activity of bismuth subsalicylate on *Clostridium difficile*, *Escherichia coli* O₁₅₇:H₇, norovirus, and other common enteric pathogens. *Gut Microbes* **2015**, *6*, 93–100. [[CrossRef](#)]
96. Song, Y.; Jiang, H.; Bi, H.; Zhong, G.; Chen, J.; Wu, Y.; Wei, W. Multifunctional Bismuth Oxychloride/Mesoporous Silica Composites for Photocatalysis, Antibacterial Test, and Simultaneous Stripping Analysis of Heavy Metals. *ACS Omega* **2018**, *3*, 973–981. [[CrossRef](#)]
97. Chen, J.; Ren, Q.F.; Ding, Y.; Xiong, C.Y.; Guo, W.M. Synthesis of bifunctional composites Ag/BiOCl/diatomite: Degradation of tetracycline and evaluation of antimicrobial activity. *J. Environ. Chem. Eng.* **2021**, *9*, 106476. [[CrossRef](#)]
98. Zhu, W.Y.; Li, Z.; Zhou, Y.; Yan, X.L. Deposition of silver nanoparticles onto two dimensional BiOCl nanodiscs for enhanced visible light photocatalytic and biocidal activities. *RSC Adv.* **2016**, *6*, 64911–64920. [[CrossRef](#)]
99. Chang, Y.; Cheng, Y.; Feng, Y.; Li, K.; Jian, H.; Zhang, H. Upshift of the d Band Center toward the Fermi Level for Promoting Silver Ion Release, Bacteria Inactivation, and Wound Healing of Alloy Silver Nanoparticles. *ACS Appl. Mater. Interfaces* **2019**, *11*, 12224–12231. [[CrossRef](#)]
100. Padervand, M.; Jalilian, E.; Majdani, R.; Goshadezahn, M. BiOCl/AgCl-BiOI/AgI quaternary nanocomposite for the efficient photodegradation of organic wastewaters and pathogenic bacteria under visible light. *J. Water Process. Eng.* **2019**, *29*, 100789. [[CrossRef](#)]
101. Gupta, G.; Kansal, S.K. Novel 3-D flower like Bi₃O₄Cl/BiOCl p-n heterojunction nanocomposite for the degradation of levofloxacin drug in aqueous phase. *Process. Saf. Environ. Prot.* **2019**, *128*, 342–352. [[CrossRef](#)]
102. Wu, D.; Ye, L.Q.; Wang, W.; Yip, H.Y.; Wong, P.K. Surfactant-free Self-Templating Construction of BiOCl/BiO_{1.84}H_{0.08} Nanodisc Heterostructures with Visible-Light-Driven Antibacterial Activity. *Chemistryselect* **2016**, *1*, 5049–5056. [[CrossRef](#)]
103. Liu, M.Y.; Zhu, H.Q.; Zhu, N.L.; Yu, Q.L. Vacancy engineering of BiOCl microspheres for efficient removal of multidrug-resistant bacteria and antibiotic-resistant genes in wastewater. *Chem. Eng. J.* **2021**, *426*, 130710. [[CrossRef](#)]
104. Chen, R.; Wei, L.; Yan, Y.; Chen, G.; Yang, X.; Liu, Y.; Zhang, M.; Liu, X.; Cheng, Y.; Sun, J.; et al. Bismuth telluride functionalized bismuth oxychloride used for enhancing antibacterial activity and wound healing efficacy with sunlight irradiation. *Biomater. Sci.* **2022**, *10*, 467–473. [[CrossRef](#)]
105. Sung, H.; Ferlay, J.; Siegel, R.L.; Laversanne, M.; Soerjomataram, I.; Jemal, A.; Bray, F. Global Cancer Statistics 2020: GLOBOCAN Estimates of Incidence and Mortality Worldwide for 36 Cancers in 185 Countries. *CA Cancer J. Clin.* **2021**, *71*, 209–249. [[CrossRef](#)]
106. Guan, S.; Wang, L.; Xu, S.M.; Yang, D.; Waterhouse, G.I.N.; Qu, X.; Zhou, S. Vacancy-enhanced generation of singlet oxygen for photodynamic therapy. *Chem. Sci.* **2019**, *10*, 2336–2341. [[CrossRef](#)]
107. Wang, Y.; Cai, D.; Wu, H.; Fu, Y.; Cao, Y.; Zhang, Y.; Wu, D.; Tian, Q.; Yang, S. Functionalized Cu₃BiS₃ nanoparticles for dual-modal imaging and targeted photothermal/photodynamic therapy. *Nanoscale* **2018**, *10*, 4452–4462. [[CrossRef](#)]
108. Xu, Y.; Shi, Z.; Zhang, L.; Brown, E.M.; Wu, A. Layered bismuth oxyhalide nanomaterials for highly efficient tumor photodynamic therapy. *Nanoscale* **2016**, *8*, 12715–12722. [[CrossRef](#)]
109. Yang, D.; Yang, G.; Li, J.; Gai, S.; He, F.; Yang, P. NIR-driven water splitting by layered bismuth oxyhalide sheets for effective photodynamic therapy. *J. Mater. Chem. B* **2017**, *5*, 4152–4161. [[CrossRef](#)]
110. Li, B.; Cheng, Y.; Zheng, R.; Wu, X.; Qi, F.; Wu, Y.; Hu, Y.; Li, X. Improving the photothermal therapy efficacy and preventing the surface oxidation of bismuth nanoparticles through the formation of a bismuth@bismuth selenide heterostructure. *J. Mater. Chem. B* **2020**, *8*, 8803–8808. [[CrossRef](#)]
111. Cheng, Y.; Chang, Y.; Feng, Y.; Jian, H.; Tang, Z.; Zhang, H. Deep-Level Defect Enhanced Photothermal Performance of Bismuth Sulfide-Gold Heterojunction Nanorods for Photothermal Therapy of Cancer Guided by Computed Tomography Imaging. *Angew. Chem. Int. Ed.* **2018**, *57*, 246–251. [[CrossRef](#)] [[PubMed](#)]
112. Ren, W.; Yan, Y.; Zeng, L.; Shi, Z.; Gong, A.; Schaaf, P.; Wang, D.; Zhao, J.; Zou, B.; Yu, H.; et al. A Near Infrared Light Triggered Hydrogenated Black TiO₂ for Cancer Photothermal Therapy. *Adv. Healthc. Mater.* **2015**, *4*, 1526–1536. [[CrossRef](#)] [[PubMed](#)]
113. Peng, C.; Liu, J.; Guo, L.; Bai, J.; Zhou, M. Oxygen vacancy-enhanced photothermal performance and reactive oxygen species generation for synergistic tumour therapy. *Chem. Commun. (Camb.)* **2020**, *56*, 11259–11262. [[CrossRef](#)] [[PubMed](#)]
114. Wang, S.; Wang, H.; Song, C.; Li, Z.; Wang, Z.; Xu, H.; Yu, W.; Peng, C.; Li, M.; Chen, Z. Synthesis of Bi₂WO_{6-x} nanodots with oxygen vacancies as an all-in-one nanoagent for simultaneous CT/IR imaging and photothermal/photodynamic therapy of tumors. *Nanoscale* **2019**, *11*, 15326–15338. [[CrossRef](#)] [[PubMed](#)]
115. Bogdan, J.; Plawinska-Czarnak, J.; Zarzynska, J. Nanoparticles of Titanium and Zinc Oxides as Novel Agents in Tumor Treatment: A Review. *Nanoscale Res. Lett* **2017**, *12*, 225. [[CrossRef](#)]
116. Yao, M.H.; Ma, M.; Chen, Y.; Jia, X.Q.; Xu, G.; Xu, H.X.; Chen, H.R.; Wu, R. Multifunctional Bi₂S₃/PLGA nanocapsule for combined HIFU/radiation therapy. *Biomaterials* **2014**, *35*, 8197–8205. [[CrossRef](#)]

117. Du, J.; Gu, Z.; Yan, L.; Yong, Y.; Yi, X.; Zhang, X.; Liu, J.; Wu, R.; Ge, C.; Chen, C.; et al. Poly(Vinylpyrrolidone)- and Selenocysteine-Modified Bi₂Se₃ Nanoparticles Enhance Radiotherapy Efficacy in Tumors and Promote Radioprotection in Normal Tissues. *Adv. Mater.* **2017**, *29*, 1701268. [[CrossRef](#)]
118. Bogusz, K.; Tehei, M.; Stewart, C.; McDonald, M.; Cardillo, D.; Lerch, M.; Corde, S.; Rosenfeld, A.; Liu, H.K.; Konstantinov, K. Synthesis of potential theranostic system consisting of methotrexate-immobilized (3-aminopropyl)trimethoxysilane coated alpha-Bi₂O₃ nanoparticles for cancer treatment. *RSC Adv.* **2014**, *4*, 24412–24419. [[CrossRef](#)]
119. Deng, J.; Xu, S.; Hu, W.; Xun, X.; Zheng, L.; Su, M. Tumor targeted, stealthy and degradable bismuth nanoparticles for enhanced X-ray radiation therapy of breast cancer. *Biomaterials* **2018**, *154*, 24–33. [[CrossRef](#)]
120. Liu, Y.; Zhang, J.; Du, J.; Song, K.; Liu, J.; Wang, X.; Li, B.; Ouyang, R.; Miao, Y.; Sun, Y.; et al. Biodegradable BiOCl platform for oxidative stress injury-enhanced chemodynamic/radiation therapy of hypoxic tumors. *Acta Biomater.* **2021**, *129*, 280–292. [[CrossRef](#)]